

## Article

# Impact of a Redox Flow Battery on the Frequency Stability of a Five-Area System Integrated with Renewable Sources

Narendra Kumar Jena <sup>1</sup>, Subhadra Sahoo <sup>1</sup>, Binod Kumar Sahu <sup>1</sup> , Amiya Kumar Naik <sup>1</sup>, Mohit Bajaj <sup>2,3,4,\*</sup> , Stanislav Misak <sup>5</sup>, Vojtech Blazek <sup>5</sup>  and Lukas Prokop <sup>5,\*</sup> 

<sup>1</sup> Department of Electrical Engineering, Siksha 'O' Anusandhan (Deemed to be University), Bhubaneswar 751024, India

<sup>2</sup> Department of Electrical Engineering, Graphic Era (Deemed to be University), Dehradun 248002, India

<sup>3</sup> Department of Electrical Engineering, Graphic Era Hill University, Dehradun 248002, India

<sup>4</sup> Applied Science Research Center, Applied Science Private University, Amman 11937, Jordan

<sup>5</sup> ENET Centre, VSB—Technical University of Ostrava, 70800 Ostrava, Czech Republic

\* Correspondence: thebestbajaj@gmail.com (M.B.); lukas.prokop@vsb.cz (L.P.)

**Abstract:** Energy storage devices are imperative to damp out the oscillations caused by sudden magnified disturbances occurring in a power system. The presence of a small rating of storage device in each area can alleviate the system oscillations effectively. Therefore, in this work, redox flow batteries (RFBs) have been integrated in each area of a five-area interconnected system for effective load frequency control (LFC). The RFB pumps up the active power into the system quickly to meet the short-time overload; in turn, the efficacy of the LFC in the system is boosted. Despite the presence of the RFB in the power system, a secondary controller is necessary to quench the deviation of frequency and tie-line power caused by the power mismatch between demand and generation. In this perspective, a cascade controller incorporated with a fractional operator (FO) has been endorsed and designed through a nascent selfish herd optimizer technique to evaluate the transient response of the system. Besides this, the unprecedented performance of fractional-order cascade controllers has been compared with one-stage classical controllers with and without a fractional operator. Further, the robustness of the proposed controller has been inspected through subjecting it to a random load in the presence/absence of an RFB and parametric variation. Finally, the proposed model has been simulated in the OPAL-RT-4510 platform to validate the performance of the proposed controller that has produced in the MATLAB environment.

**Keywords:** load frequency control; fractional order controller; cascade controller; selfish herd optimizer; robustness analysis; redox flow battery; Li-ion battery



**Citation:** Jena, N.K.; Sahoo, S.; Sahu, B.K.; Naik, A.K.; Bajaj, M.; Misak, S.; Blazek, V.; Prokop, L. Impact of a Redox Flow Battery on the Frequency Stability of a Five-Area System Integrated with Renewable Sources. *Energies* **2023**, *16*, 5540. <https://doi.org/10.3390/en16145540>

Academic Editor: Wajiha Shireen

Received: 12 May 2023

Revised: 4 July 2023

Accepted: 19 July 2023

Published: 21 July 2023



**Copyright:** © 2023 by the authors. Licensee MDPI, Basel, Switzerland. This article is an open access article distributed under the terms and conditions of the Creative Commons Attribution (CC BY) license (<https://creativecommons.org/licenses/by/4.0/>).

## 1. Introduction

An interconnected upgraded power system comprises many control areas for the exchange of scheduled power through interconnected tie-lines. Due to the incessant rise and abrupt power demand of a bulky, complex and nonlinearity-containing electric network, it is not quite easy to adhere the system frequency and tie-line power to a set value. If the frequency excursion lies under an acceptable tolerance value [1], then the system can fulfil the consumer's need through serving secure, reliable and quality power. Under this condition, the synchronization between the interconnected areas remains unaltered. If the deviation in frequency is sustained for a longer period and/or with an unwanted magnitude, then the system performance gets worse, culminating in a blackout. Besides this, the magnetizing current of the transformer and induction machine increases sharply. The fluctuation in frequency also badly hampers timing devices. So, for the smooth and stable operation of a power system, the mismatch between power demand and generation must be narrowed [1,2]. The aforesaid problem is continuously traced using an automatic generation control (AGC) system. During normal and abnormal conditions, AGC damps

out the oscillation contents present in frequency and tie-line power deviation signals, and, in turn, dynamic performance and stability are improved. The control action of AGC contributes in two stages. In the first action, AGC controls the frequency deviation with the help of the governor and turbine, due to which a steady-state error may remain. But via the complementary control action, it brings the deviation of frequency to zero with the help of different employed controllers. So, researchers are paying more attention to the design of an apposite controller which plays a key role in bringing the area control error to zero.

The presence of unavoidable non-linearities in the system is a very critical factor due to which the power and frequency signals oscillate. In this regard, the effect of the dead band [3,4] on system dynamics has been explained explicitly for different interconnected electrical networks. Another nonlinear quantity, namely, generation rate constraint (GRC), has been included in the study of a three unequal area thermal system as analysed by Nanda et al. [5]. Similarly, both GRC and GDB have been integrated to investigate the AGC issue in a two-area thermal system by Gozde et al. [6]. Morsali et al. [7] proposed an AGC system considering both GDB and GRC nonlinearity and also analysed their impact on stability. Saikia et al. [8] carried out a study of AGC in a five equal area system having thermal units with GRC. Jagatheesan et al. [9] studied AGC for a two, three and four equal area power system. Bhatt et al. [10] studied an AGC system keeping three kinds of diversified sources such as hydro, thermal and diesel. So, the problem introduced by nonlinearities to the system can be mitigated using a suitable and well-designed controller.

For the last few decades, the PID controller has carved a well-established space in modern industries profusely due to its easy implementation and simple structure. A minute review of the LFC problem has been presented by Pandey et al. [11]. Elgerd and Fosha [12] endowed an integral (I) controller in a multi-area system to stabilize the frequency. Nayak et al. [13] proposed a comparative study of AGC in a multi-area system using PID and its variants using fuzzy logic. An optimal PID controller has been designed for an LFC study in a multi-area system, which shows dominant performance over other controllers as described by Guha et al. [14]. Nanda et al. [5] worked on PID and its verities in an AGC issue for a hydro-thermal multi-area energy system. Recently, Gouran-Orimi et al. [15] addressed the effectiveness of a PID controller to tackle the LFC problem in a system having renewable sources. Here, the sturdiness of this controller has been analysed with respect to a wide variation of uncertainties, which cannot be guaranteed. To improve the performance of an electric power system, Sahu et al. [16] proposed a two-degrees-of-freedom PID controller and also cited the performance in comparison to various kinds of PID controllers. But the curious minds of researchers never stall at only PID controllers. There are also non-integer or fractional order controllers; the combination of PID controllers arrayed in two stages, named cascade controllers; and many more. In this perspective, Alomoush [17] elaborated the superiority of non-integer-based controllers over integer-based controllers. Morsali et al. [18] capitalized on an FO-PID controller for AGC in a multisource multi-area system. Zamani et al. [19] designed an FO-PID controller to study the LFC in a two-area system. Besides this, a two-stage-based controller helps researchers to bring the area control error to zero in such a way that the dynamic response of the system becomes faster and the steady-state error gets narrower. In this respect, Annamraju et al. [20] employed a PD-PI controller coordinated with a fractional operator for AGC in a micro-grid. Jena et al. [21] proposed an FO-cascade controller with a derivative filter in a three-area system under deregulated conditions. Sivalingam et al. [22] used a PDN plus (1 + PI) cascade controller for an AGC study in two-area and three-area systems. Saha et al. [23] studied the performance of the AGC of a power system in the presence of an energy-storing element, applying two degrees of freedom to support the PIDN-FOI two-stage controller. Arya [24] studied the AGC of a multi-area system employing a multistage controller aided with fuzzy logic named the FPIDF-(1 + PI) controller. A 2DOF-based PI-FOPDN cascade controller was used by Prakash et al. [25] to investigate AGC issues in the restructured power system. Recently, Pahadasingh et al. [26] illustrated that the cascade controller has great potential to regulate the frequency in a system integrated with an electric vehicle. Similarly, Mao et al. [27]

described the impact of energy storing components on a system in the coordination of cascade controllers. To the best of our knowledge, FOPIDN-FOPDN is one of the novel controllers yet to be designed for the study of LFC in a five-area system. This curiosity compels the authors to use a cascade controller for LFC issues.

Despite a pertinent and effective controller, the oscillations in the system are a critical issue during large disturbances that occurs in a non-linear and intricate system. To alleviate these oscillations, fast active power injection is necessary. In this perspective, an RFB is chosen as a very crucial and influential energy source to mitigate these oscillations, through which the quality and reliability of the power increase. Generally, conventional storage systems like lithium-ion battery systems require high maintenance, lack safety features, face material unavailability, are toxic to the environment and non-recyclable, which encourages researchers to find a competent alternative. For this, the RFB is the most suitable storage system, as discussed in [28], to use in a large scale, which has attracted researchers immensely. The key features of the RFB are illustrated below:

- i. Storage capacity, both in power and energy, is very high.
- ii. Unlike other storage devices, power and energy are independent entities in the RFB system. Here, energy capacity depends on the electrolyte reservoir and power capacity depends on the stack size.
- iii. The heat produced by redox reactions is dissipated by the electrolytes, which is a major advantage over solid-state storages.
- iv. The manufacturing process is modular, which is quite different from solid-state batteries like those manufactured in the form of cell.
- v. The life cycle is long and efficiency is high.

In spite of some disadvantages, like the addition of complexity to the system, low energy density and the difficult handling of corrosives in the electrodes, the RFB is more valuable to employ in a power system to support the stability of the power system. In this respect, Arya [29] has illustrated the contribution of RFBs in a power system. In this paper, it has been cited that the RFB has curtailed oscillations and, also, the LFC issue has been boosted. Similar kind of work has been carried out by Ramesh et al. [30] to improve the dynamic response of a deregulated system using an RFB device. Besides this, some recent works [31–35] have eloquently illustrated the impact and effectiveness of RFB in different systems under different circumstances.

To achieve a better response of a system, a well-designed controller is necessary. The gains should be enumerated tightly, through which the dynamic response is faster and ACE decreases to zero. So, a suitable computational technique is essential. It has been observed that not all kinds of computational algorithms are suitable for the optimization of a particular problem as stated by Wolpert et al. [36]. So, different authors are proposing and applying different algorithms to different types of problems. Abubakr et al. [37] used Jaya optimization to study LFC in a micro-grid under a variable-time-delay condition. In this work, this optimization is modified via the balloon effect modulation technique. Bhatt et al. [10] carried out the study of AGC in a multi-unit system using the GA and particle swarm optimization techniques. The firefly algorithm has been implemented for the LFC of a multi-area system by Sarma et al. [38]. A fuzzy-PID controller has been designed in [39] using a teaching–learning-based computational algorithm employed in a multi-area system for automatic generation control. Pradhan et al. [40] proposed modified Jaya optimization to investigate LFC in an integrated wind energy system. So, in this work, a selfish herd optimizer (SHO) [41], a bio-inspired algorithm, has been proposed.

Through applying the computational technique, the dynamic and transient response of a system improves substantially. To establish the improvement of undershoot, overshoot and settling time, the time response is imposed on a cost function. In this perspective, different papers [42–45] have discussed the optimum solution evaluation through different cost functions. The integral square error (ISE) index cost function has been applied in [42] to minimize the error of the system. Similarly, Abdel-Magid et al. [43] used the objective function ISE and integral time square error (ITSE) functions to enhance the stability of the

proposed system with their advantages. Here, it has been cited that the ITSE index-based performance side-lines the ISE based performance. Gozde et al. [44] proposed integral absolute error (IAE), ITSE, ISE and integral time absolute error (ITAE) indexed functions to optimize PI and PD controllers using an artificial bee colony in an interconnected reheat thermal system for automatic generation control. Shabani et al. [45] developed an optimal PID controller optimized using an ICA algorithm subjecting ITAE, IAE and ISE cost functions to the LFC of an interconnected power system, and the ITAE-indexed function superseded the rest of the cost functions. In the purview of error minimization, ITAE cost function has been endorsed to enumerate the gains of the proposed controllers.

From the literature, it is reported that in a five-area system, all the three nonlinearities, i.e., GRC, GDB and boiler dynamics, have not addressed. Secondly, few papers have addressed the impact of a two-stage controller coordinated using fractional operators. So, more exploration of fractional-based cascade controllers is necessary. Regarding these aspects, in this work, the AGC of a five-area test system containing diversified sources and subjected to all sorts of non-linearities has been addressed.

The main contributions of this paper are as follows:

- a. A five-area test model having two sources in each area is modelled incorporating GRC, GDB and boiler dynamics to make the interconnected power system more practical.
- b. A two-stage non-integer controller, FOPIDN-FOPDN, is designed by means of conglomerating a derivative filter which neutralizes the distorted signals generated by the system. Additionally, the performance of this controller is compared with PID and FOPID controllers.
- c. A nascent optimization algorithm selfish herd optimisation (SHO) is applied to tune the gain parameters of the aforementioned controllers. With this, the potential of the SHO algorithm and its performance have been compared with PSO through some benchmark functions.
- d. The performance of the test model under RFB has been evaluated and compared with another BESS system.
- e. The robustness of the designed controller is analysed via imposing different load conditions with/without an RFB, and finally, a sensitivity analysis has been presented through varying some crucial system parameters.
- f. The feasibility of the proposed controller is examined through simulating through a real-time simulator (OPAL-RT-4510).

The remaining sections of this work are kept as follows. Section 2 describes the linearized model of the five equal area interconnected power system. Besides this, all the nonlinear models have been presented in this section. In Section 3, the proposed controller, along with its counterpart controllers, is described. A formulation of the problem is given in Section 4. The SHO algorithm is emulated in Section 5. The performance of SHO over PSO during benchmark functions is presented in Section 6. Simulation results, transient data, controller gain values and their analysis are presented in Section 7. The conclusion and futuristic development of this work are given in Section 8.

## 2. Linearized Model of the Investigated System

Here, a five-area multi-source test model is considered for the study of AGC, and its linearized model is portrayed in Figure 1. The first area comprises two conventional units such as a thermal unit and a hydro unit. A hydro unit along with a wind farm is taken in area-2. The third area is integrated with a thermal unit and a diesel unit. A thermal unit combined with a gas unit is injected into the fourth area. The fifth area carries a thermal unit along with a nuclear unit. In this work, non-linearities such as GRC and GDB are endorsed in thermal and hydro units to make the power system more practical. Besides this, boiler dynamics are also included in the thermal unit in the concerned areas. The linearised models and the required parameters of the hydro-thermal unit are referred from [39]. The modelling of the gas unit, GDB and GRC used in hydro and reheat thermal units is inherited from [7]. The boiler dynamics in the thermal unit are taken from [3] and are presented in

Figure 2a. The linearized model of a wind farm and diesel unit is adopted from [14]. The modelling of the nuclear unit in the Laplace domain and its required parameters are taken from [46]. The transfer function model of the nuclear unit is depicted in Appendix A, and its simplified expression is presented in the nuclear block, as shown in Figure 1.

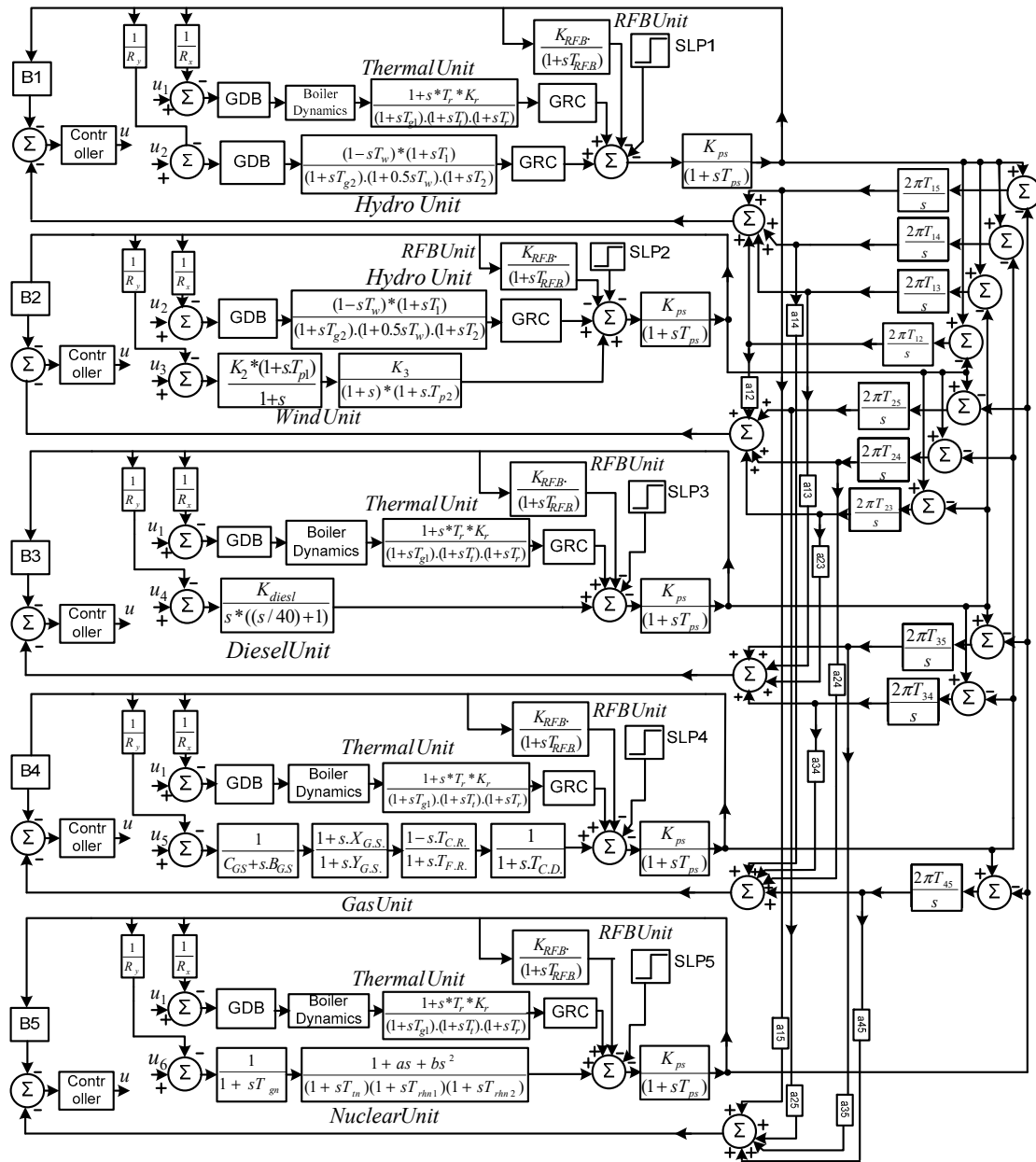


Figure 1. Model of a five-area interconnected power system.

### 2.1. Redox Flow Battery (RFB)

The RFB is a very promising storage device to deliver active power into the network under highly perturbed conditions. Due to some attractive features like high efficiency, flexible capacity increase, resistance to deterioration from frequent charging/discharging, more economical properties, etc., it has been used abundantly in recent years. An RFB can be designed to produce energy from some KW to a few MW [29]. Also, it is free from self-discharge as the electrolytes are kept in separate containers. In practice, the RFB is a non-linear device, but from the simplification angle, it is linearised, which is provided

in Figure 1. The parameters of this storage device have been taken from [29,30] and are presented in Appendix A.

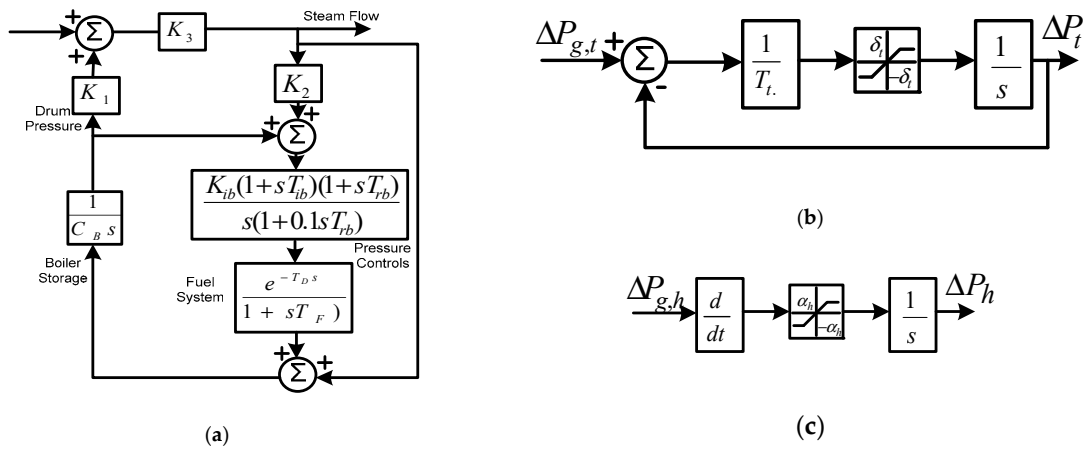


Figure 2. (a) Model of boiler, (b) model of GRC for thermal unit and (c) model of GRC for hydro unit.

### 2.2. Generation Rate Constraint (GRC)

Power generation, which follows a specified maximum rate, cannot be changed suddenly. If this constraint is not considered, then the system introduces momentary disturbances which increase the instability of the system. Here, the GRC is considered for both thermal and hydro units. The maximum rate of valve opening and closing speed is restricted by the limiter, such as for raising/lowering the power generation. In a hydro unit, for generation raising/lowering, a GRC of 270%/min and  $-360\%/min$  as in [14] is considered, respectively. Like hydro units, in thermal units, a  $\pm 3\%/min$  GRC rate as in [14] is considered. The GRC model is shown in Figure 2b,c.

### 2.3. Boiler Dynamics

Boiler dynamics are included in the thermal unit to study the effect produced by the flow of fuel and steam inside the boiler under pressure. In this work, a drum-type boiler is taken as reported in [3]. The drum is used to separate the steam flow from the circulated water and feeds to the super-heater. A sensor senses the changes in steam flow and deviation in pressure, and the turbine control valve and boiler controller take the corresponding action. A block diagram of boiler dynamics configuration is shown in Figure 2a.

### 2.4. Governor Dead Band (GDB)

The GDB is a band (range/magnitude) of speed change irrespective of valve position change. It is articulated by means of a descriptive function incurring sustained oscillation. The natural frequency of this sustained oscillation is  $f_0 = 0.5$  Hz as illustrated by Tripathy et al. [3]. The described function has been explained below.

$$y_o = F(z, z') \tag{1}$$

$$z = M * \sin(\omega_0 \cdot t) \tag{2}$$

where  $M$  and  $\omega_0 = 2\pi f_0$  are magnitude and natural frequency (rad/s), respectively. The Fourier expansion is given as follows:

$$F(z, z') = F_0 + N_1 z + \frac{N_2}{\omega_0} z' + \dots \tag{3}$$

Here,  $F_0 = 0$  because the backlash is symmetrical about the origin. Restricting up to the first order, Equation (3) is approximated as given in Equation (4).

$$F(z, z') = N_1 z + \frac{N_2}{\omega_0} z' = \left( N_1 + \frac{N_2}{\omega_0} \frac{d}{dt} \right) z = DBz \tag{4}$$

where  $DB$  stands for the dead band. The following parameters are chosen as prescribed in [3]:  $backlash = 0.05\%$ ,  $N_1 = 0.8$  and  $N_2 = -0.2$ .

### 3. Control Strategies Adopted for the Study

#### 3.1. PID Controller

The classical PID controller is an omnipresent controller which is very simple in structure, reliable to implement and popularly stands at its own niche. Despite the advent of new technologies, it is still used profusely in modern industries. The performance of the PID controller is far better than its varieties, PI and I. The PID controller is shown in Figure 3a, and its expression is given in Equation (5).

$$G(s) = k_{p_x} + \frac{k_{i_x}}{s} + k_{d_x} s \tag{5}$$

$x$  stands for the number of controllers.

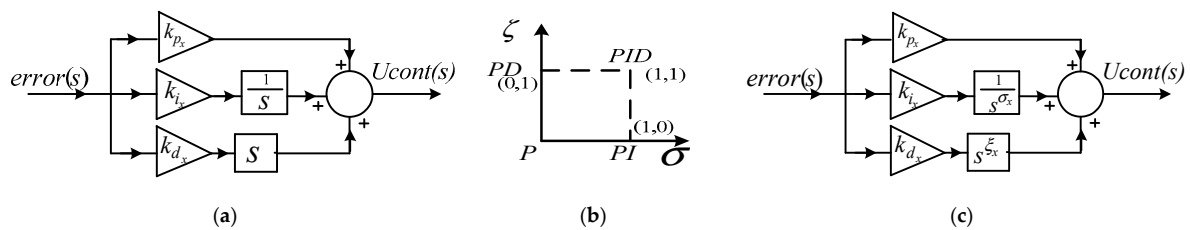


**Figure 3.** (a) PID controller, (b) working region of PID and FOPID and (c) FOPID controller.

#### 3.2. Fractional Order Controller

The non-integer calculus concept rose by L'Hospital for  $n = 0.5$  to Leib-niz, created a space for the next generation to evolve FO-calculus. A maiden attempt has been taken by Podlubny [46] to implement a  $PI^\alpha D^\zeta$  controller exploring a non-integer order integrator and differentiator. Though it has five parameters to be tuned, due to non-integer order integro-differentiation accompanied by integer order gains, it is quite flexible for ascertaining spectacular performance with these gains. The non-integer calculus is provided in Equation (6).

$$a^D_t^q = \begin{cases} \frac{d^q}{dt^q} & ; for, q > 0 \\ 1 & ; for, q = 0 \\ \int_a^t (d\tau)^{-q} & ; for, q < 0 \end{cases} \tag{6}$$

In Caputo form, i.e., when Equation (6) is applied to a function, then Equation (7) is formed.

$$a^D_t^q = \begin{cases} \frac{1}{\Gamma(m-q)} * \int_a^t \frac{f^m(\tau)}{(t-\tau)^{(q+1-m)}} \cdot d\tau & ; (m-1) < q < m \\ \frac{d^m}{dt^m} (f(t)) & ; q = m \end{cases} \tag{7}$$

where ' $\Gamma$ ' is a Gamma function, ' $a$ ' and ' $t$ ' are the limits of the function, ' $q$ ' is the order of the calculus and  $m > q$ . With the initial condition equal to zero, the Laplace transformation of non-integer derivatives and integration are provided in Equations (8) and (9).

$$L\left(0^{D_t^q} f(t)\right) = s^q F(s) - [0^{D_t^{q-1}} f(t)]_{t=0} \quad (8)$$

$$L\left(0^{D_t^{-q}} f(t)\right) = s^{-q} F(s) \quad (9)$$

The solution of the fractional order function is carried out via a numerical approximation [47], which is given in Equation (10).

$$s^q = K * \prod_{n=1}^N \left( \frac{1 + s/\omega_{z,n}}{1 + s/\omega_{p,n}} \right) : q > 0 \quad (10)$$

The defined function in Equation (10), having gain of  $K$ , has  $N$  number of poles and zeros lying in a frequency band of  $[\omega_l \ \omega_n]$ .  $N$  value is chosen to make the fractional order function solution less complex with subsiding ripple contents in the gain and phase of the solution. The corner frequencies (poles/zeros) of the function are given as follows:

$$\omega_{z,n} = \omega_l \cdot \sqrt{n} \quad (11)$$

$$\omega_{p,n} = \omega_{z,n} \cdot \varepsilon \quad (12)$$

$$\omega_{z,n+1} = \omega_{p,n} \cdot \sqrt{\eta} \quad (13)$$

$$\eta = \left( \frac{\omega_n}{\omega_l} \right)^{(1-q)/N} \quad (14)$$

$$\varepsilon = \left( \frac{\omega_n}{\omega_l} \right)^{q/N} \quad (15)$$

It is important to notice that Equation (10) becomes rational for  $|q| > 1$ . Under this condition, the Oustaloup approximation [47] does not fit well. So, a complex frequency with power  $q$  is decomposed as:

$$s^q = s^n * s^\sigma \quad (16)$$

where  $n \in z$  and  $q = n + \sigma$ . Additionally,  $s^\sigma$  is approximated, keeping the corner frequencies in between 0.01 rad/s and 100 rad/s, as demonstrated in [48].

The area under the dashed line in Figure 3b is meant for the FO calculus and the corner points stand for the integer calculus. The additive features of FO in comparison to the integer one ease the stability of linear/nonlinear systems adequately. In the  $PI^\sigma D^\zeta$  controller,  $\sigma$  and  $\zeta$  are the FO parameters, and its control signal is given in Equation (17).

$$u(t) = k_{p_x} \cdot e(t) + k_{i_x} \cdot D_t^\sigma(e(t)) + k_{d_x} \cdot D_t^\zeta(e(t)) \quad (17)$$

where  $x =$  controllers (1, 2, ..., 5) and  $e(t)$  is the error signal.

From Figure 3c, the transfer function of the controller is given in Equation (18).

$$G(s) = k_{p_x} + \frac{k_{i_x}}{s^{\sigma_x}} + k_{d_x} \cdot s^{\zeta_x} \quad (18)$$

### 3.3. Cascade Controller

Due to the moderate performance of the PID controller employed in a higher-order system with nonlinearities, two-stage PID controllers have been evolved to get rid of the mentioned problem. So, in this work, PIDN and PDN controllers incorporating non-integer calculus have been cascaded to form a FOPIDN-FOPDN controller. The control structure is portrayed in Figure 4.

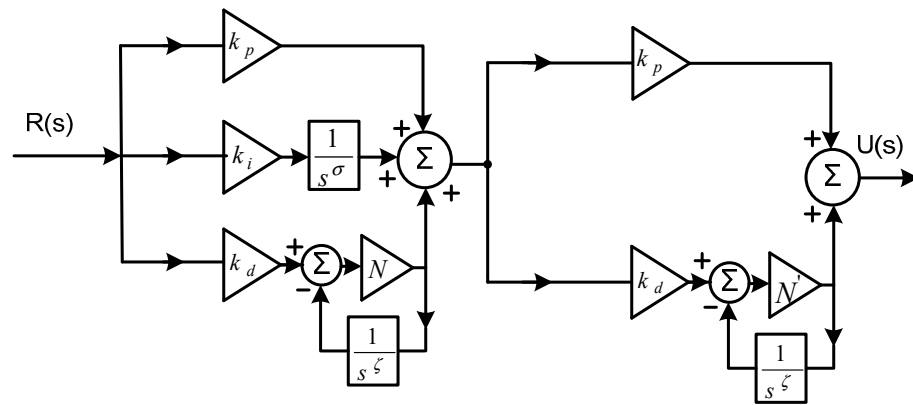


Figure 4. FOPIDN-FOPDN controller.

The integer-based cascade controller modelling is expressed as given below. The transfer functions for *PIDN* and *PDN* control structures are

$$G_1(s) = k_{p_x} + \frac{k_{i_x}}{s} + k_{d_x} \cdot s \left( \frac{N}{N+s} \right) \text{ and}$$

$$G_2(s) = k_{p_x} + k_{d_x} \cdot s \left( \frac{N}{N+s} \right), \text{ respectively.}$$

So, the overall transfer function for the *PIDN* – *PDN* controller is formulated in Equation (19).

$$G(s) = G_1(s) * G_2(s) = \left\{ k_{p_x} + \frac{k_{i_x}}{s} + k_{d_x} \cdot s \left( \frac{N}{N+s} \right) \right\} \left\{ k_{p_x} + k_{d_x} \cdot s \left( \frac{N}{N+s} \right) \right\} \quad (19)$$

From Figure 4, the transfer functions of  $PI^\sigma D^\zeta N$  and  $PD^\zeta N$  are written as

$$G_1(s) = k_{p_x} + k_{i_x} \cdot s^{-\sigma} + k_{d_x} \cdot s^\zeta \left( \frac{N}{N+s^\zeta} \right) \text{ and}$$

$$G_2(s) = k_{p_x} + k_{d_x} \cdot s^\zeta \left( \frac{N}{N+s^\zeta} \right), \text{ respectively.}$$

The overall transfer function is given below:

$$G(s) = G_1(s) * G_2(s) = \left\{ k_{p_x} + k_{i_x} \cdot s^{-\sigma} + k_{d_x} \cdot s^\zeta \left( \frac{N}{N+s^\zeta} \right) \right\} \left\{ k_{p_x} + k_{d_x} \cdot s^\zeta \left( \frac{N}{N+s^\zeta} \right) \right\} \quad (20)$$

#### 4. Mathematical Problem Formulation

The presided five area interconnected system comprises six distinct diversified sources as depicted in Figure 1. The system is investigated through imposing three varieties of controllers such as PID, FOPID and FOPIDN-FOPDN controllers and employing six controllers, one for each type of generating unit. The gains of these controllers are calculated optimally using an emerging SHO soft-computing technique. A step load perturbation of 1% is imposed in the first area to examine the excursion of frequency and tie-line power of the proposed system. To achieve better control through minimizing the area control error, a time domain integral performance is applied. In this paper, an ITAE-indexed cost function is chosen to find the optimal gains of the proposed controllers. The fitness function 'J' is given below.

$$J_{\text{cost}} = \int_0^t \left[ \begin{aligned} &|\Delta f_1| + |\Delta f_2| + |\Delta f_3| + |\Delta f_4| + |\Delta f_5| + |\Delta Ptie_{1,2}| + |\Delta Ptie_{2,3}| + \\ &|\Delta Ptie_{3,4}| + |\Delta Ptie_{4,5}| + |\Delta Ptie_{5,1}| \end{aligned} \right] * t dt \quad (21)$$

And the constraints for the minimization of the cost function ( $J_{\text{cost}}$ ) are given below.

$$k_{p_x, \min} \leq k_{p_x} \leq k_{p_x, \max}, k_{i_x, \min} \leq k_{i_x} \leq k_{i_x, \max}, k_{d_x, \min} \leq k_{d_x} \leq k_{d_x, \max}, \\ \sigma_{x, \min} \leq \sigma_x \leq \sigma_{x, \max}, \zeta_{x, \min} \leq \zeta_x \leq \zeta_{x, \max}, N_{x, \min} \leq N_x \leq N_{x, \max}$$

where  $k_{PID,x(\min)}$  and  $k_{PID,x(\max)}$  are between 0 and 5,  $\sigma_{FOPID,x(\min)}$  and  $\sigma_{FOPID,x(\max)}$  are in the range (0, 1),  $\zeta_{FOPID,x(\min)}$  and  $\zeta_{FOPID,x(\max)}$  are in the interval of (0, 1) and the derivative filter coefficients are in between 20 and 200.

### 5. Selfish Herd Optimizer

Dating back to 1971, Hamilton proposed a bio-inspired theory of the selfish herd, which was further developed into an optimization technique by Fausto et al. [40] named SHO. This model projects the gregarious conduct of organisms to accumulate benefits mutually among themselves. From this perspective, it can be conceptualized that whenever a predator attacks, everyone in the herd tries not to fall into predation through seeking to be in a safe shield. Also, they never intentionally cause the other organisms to fall in danger. So, the risk of predation is greater at the periphery and less at the centre. The strongest organism occupies the centre position and the weaker are laid at the periphery. This phenomenon is articulated in the SHO program as described in different steps below.

#### 5.1. Initialization Phase

The population count (N), iteration count (itermax), lower limit  $x_m^{low}$  and upper limit  $x_m^{high}$  are set before the initiation of this phase. A set of populations of animals  $A = \{a_1, a_2, \dots, a_N\}$  are initialized randomly within the specified limits using Equation (22).

$$a_{l,m}^0 = x_m^{low} + rand(0, 1) \cdot (x_m^{high} - x_m^{low}) \tag{22}$$

where  $l = (1, 2, \dots, N)$  and  $m = (1, 2, \dots, n)$ .

The herd is separated into prey ( $N_h$ ) and predator ( $N_p$ ) using the following relations:

$$N_h = floor(N \cdot rand(0.7, 0.9))$$

$$N_p = N - N_h$$

The survival value of each animal is determined as follows:

$$SV_{al} = \frac{f(a_l) - f_B}{f_B - f_W} \tag{23}$$

where  $f_B$  and  $f_W$  are evaluated as:

$$f_B = \min_{m=\{0,1\dots k\}} \left( \left( \min_{l=\{1,2\dots N\}} (f(a_l)) \right)_m \right)$$

$$f_W = \max_{m=\{0,1\dots k\}} \left( \left( \max_{l=\{1,2\dots N\}} (f(a_l)) \right)_m \right)$$

#### 5.2. Structurization Phase

The leader ( $h_L$ ) has minimum survival value (SV), and the organisms with a greater SV than the leader are the nearest neighbours ( $h_N$ ).

$$h_L^K = \left( h_l^k \in H^k \mid SV_{h_l^k} = \max_{m=\{1,2,\dots,N_h\}} (SV_{h_m^k}) \right) \tag{24}$$

$$h_{N_m}^k = \left( h_m^k \in H^k, h_m^k \neq [h_l^k, h_L^k] \mid SV_{h_m^k} > SV_{h_l^k}, r_{lm} = \min_{m=\{1,2,\dots,N_h\}} (\|h_l^k - h_m^k\|) \right) \tag{25}$$

The organisms in the herd, excluding the leader, are fragmented into followers ( $H_F^k$ ) and deserters ( $H_D^k$ ).

$$H_F^k = \left\{ h_l^k \neq h_L^k \mid SV_{h_l^k} \geq \text{rand}(0,1) \right\} \quad (26)$$

$$H_D^k = \left\{ h_l^k \neq h_L^k \mid SV_{h_l^k} \geq \text{rand}(0,1) \right\} \quad (27)$$

Again, depending on their survival value, the follower organisms are fragmented into dominant herd members and subordinate herd members.

$$H_d^k = \left\{ h_l^k \in H_F^k \mid SV_{h_l^k} \geq SV_{H_\mu^k} \right\} \quad (28)$$

$$H_s^k = \left\{ h_l^k \in H_F^k \mid SV_{h_l^k} < SV_{H_\mu^k} \right\} \quad (29)$$

where  $SV_{H_\mu^k} = \frac{\sum_{l=1}^{N_h} SV_{h_l^k}}{N_h}$ .

The centre of mass gives the degree of safety for the position of the herd and predator groups as given in Equations (29) and (30).

$$h_M^k = \frac{\sum_{l=1}^{N_h} SV_{h_l^k} \cdot h_l^k}{\sum_{m=1}^{N_h} SV_{h_m^k}} \quad (30)$$

$$p_M^k = \frac{\sum_{l=1}^{N_p} SV_{p_l^k} \cdot p_l^k}{\sum_{m=1}^{N_p} SV_{p_m^k}} \quad (31)$$

### 5.3. Movement Phase of Herd

In this phase, movement of the leader of the herd and the followers as well as the desertion of the herd have been evaluated considering their SV value and the distance from other organisms. This phenomenon has been described in terms of attraction and repulsion operators as in Equations (32) and (33). Additionally, the position of the leader is evaluated by Equation (34).

$$\psi_{h_l, h_m} = SV_{h_m} \cdot e^{-\|h_l - h_m\|^2} \quad (32)$$

$$\varphi_{h_l, p_M} = -SV_{p_M} \cdot e^{-\|h_l - p_M\|^2} \quad (33)$$

$$h_L^{k+1} = \begin{cases} h_L^k + c^k & \text{if } SV_{h_L^k} = 0 \\ h_L^k + s^k & \text{if } SV_{h_L^k} > 0 \end{cases} \quad (34)$$

where  $c^k = 2 \cdot \alpha \cdot \phi_{h_L, p_M}^k \cdot (p_M^k - h_L^k)$  and  $s^k = 2 \cdot \alpha \cdot \psi_{h_L, x_{best}}^k \cdot (x_{best}^k - h_L^k)$ . The positions of other members are updated according to Formula (35).

$$h_l^{k+1} = \begin{cases} h_l^k + f_l^k & \text{if } h_l^k \in H_F^k \\ h_l^k + d_l^k & \text{if } h_l^k \in H_D^k \end{cases} \quad (35)$$

### 5.4. Movement Phase of Predator

Generally, a predator attacks the prey (selfish herd) which is more vulnerable. This is decided on the basis of the relative position between the predator and the herd member (prey) to be attacked. So, this attribute has been defined by the SHO algorithm in the movement phase of the predator. Here, the distance of the predator to the herd (prey) and the survival aptitude of the herd to be hunted play a key role. This is expressed as

the pursuit probability, as given in Equation (36), between the predator and the herd to be hunted.

$$P_{p_l h_m} = \frac{\omega_{p_l h_m}}{\sum_{m=1}^{N_h} \omega_{p_l h_m}} \quad (36)$$

These members update their position as

$$p_l^{k+1} = p_l^k + 2\rho(h_r^k - p_l^k) \quad (37)$$

### 5.5. Predation Phase

The radius of the domain of danger and the threatened prey are calculated as:

$$R = \frac{\sum_{m=1}^n |x_m^{low} - x_m^{high}|}{2 \cdot n} \quad (38)$$

Threatened prey of a given predator is determined accordingly:

$$T_{p_l} = \{h_m \in H | SV_{h_m} < SV_{p_l}, \|p_l - h_m\| \leq R, h_m \notin K\} \quad (39)$$

where  $K$  is a null set.

The members of the threatened prey are being hunted according to the probability, determined by

$$H_{p_l, h_m} = \frac{\omega_{p_l, h_m}}{\sum_{(h_m \in T_{p_l})} \omega_{p_l, h_m}}, h_m \in T_{p_l}$$

The killed members are kept in a set  $K$  such that

$$K = \{K_l = (h_m \in H)\}, \text{ for } l = 1, 2, \dots, N_k \text{ \& } m = 1, 2, \dots, N_h. \quad (40)$$

### 5.6. Restoration Phase

In this step, new organisms are added to keep the herd group size constant. The new members are generated based on mating probability (MB) as given in Equation (41).

$$M_{h_m} = \frac{SV_{h_l}}{\sum_{(h_m \in M)} SV_{h_m}}, h_m \in M \quad (41)$$

To interchange the positions among 'n' number of individuals selected randomly from the matrix 'M', the roulette selection procedure is applied for MB. Following the whole process, a solution is generated. Further, the generation of new solutions is continued until the defined criteria.

#### **Pseudocode for SHO:**

##### **# Initialisation #**

Initialize the population randomly within the search range and evaluate the performance of each prey using Equation (23).

Form = 1:Maximum number of iterations

for  $l = 1$ :Number of prey

Divide the organisms/population into Herd and Predator groups.

Determine the centre of mass of herd and predator using Equations (30) and (31) respectively.

Calculate the force of attraction among the members of herd group from Equation (32).

Calculate the force of repulsion between the members of herd & predator using Equation (33).

##### **# Updation of members of herd group#**

Identify the leader of herd group and update its position using Equation (34).

Update the other members of the herd group using Equation (35).

##### **# Updation of members of predator group #**

Determine the pursuit probability of each predator using Equation (36).

Update the members of predator group using Equation (37).

**# Predation Phase #**

Determine the radius of the domain of danger using Equation (38).

Determine the set of threatened prey from Equation (39).

Determine the probability of threatened prey being hunted by a predator.

Identify the prey to be killed by the predator using Roulette wheel selection criteria.

Replace the killed prey by randomly generated prey within the search range.

End

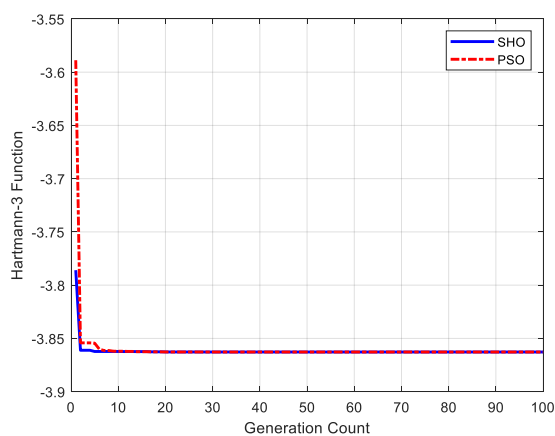
end

**6. Proficiency of SHO over PSO through Benchmark Function Analysis**

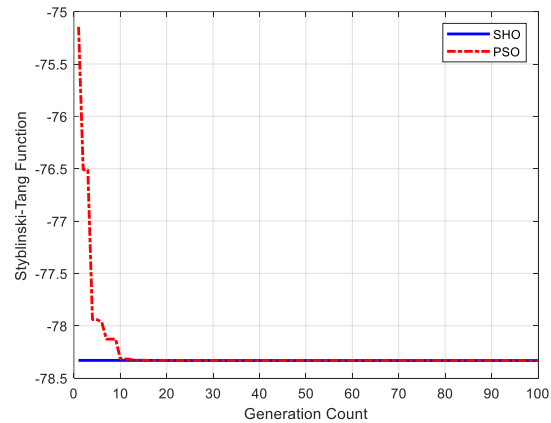
To advocate the use of a new algorithm, SHO, over PSO, the potential of these algorithms has been evaluated and compared through some benchmark functions. These functions have been provided in Table 1. Each function’s search space and dimensions have been implemented. The convergence graphs of these functions for SHO and PSO have been shown in Figure 5. From these curves, it is evident that SHO has gained its appreciation to for better convergence. Different specifications like optimum, minimum, maximum, mean, standard deviation and computational time have been calculated and presented in Table 2. From the table data, it is clear that the minimum and maximum almost match the optimum value produced by both SHO and PSO algorithms. But, the computational time is longer for the SHO algorithm as the algorithm is executed through five different steps as discussed in the previous section. Also, the standard deviation produced by the SHO algorithm is very low in comparison to the PSO algorithm.

**Table 1.** Benchmark functions with it’s dimensions and search space.

Name	Expression	Dimensions (d)	Search Space
Hartmann	$f(x) = -\sum_{i=1}^4 \alpha_i * \exp\left(-\sum_{j=1}^3 A_{ij}(x_j - P_{ij})^2\right)$	3	[0, 1]
Styblinski-Tang	$f(x) = \frac{1}{2} \sum_{i=1}^d (x_i^4 - 16x_i^2 + 5x_i)$	2	[5, 5]
Rotated hyper-ellipsoid	$f(x) = \sum_{i=1}^d \sum_{j=1}^i (x_j^2)$	2	[-65.536, 65.536]
Schaffer	$f(x) = 0.5 + \frac{\cos^2(\sin( x_1^2 - x_2^2 )) - 0.5}{[1 + 0.001 * ( x_1^2 + x_2^2 )]^2}$	2	[-100, 100]
Mccormick	$f(x) = \sin(x_1 + x_2) + (x_1 - x_2)^2 - 1.5 * x_1 + 2.5 * x_2 + 1$	2	$x_1 \in [-1.5, 4]$ $x_2 \in [-3, 4]$
Sum-Squares	$f(x) = \sum_{i=1}^d i * x_i^2$	2	[-10, 10]



(a)



(b)

**Figure 5.** Cont.

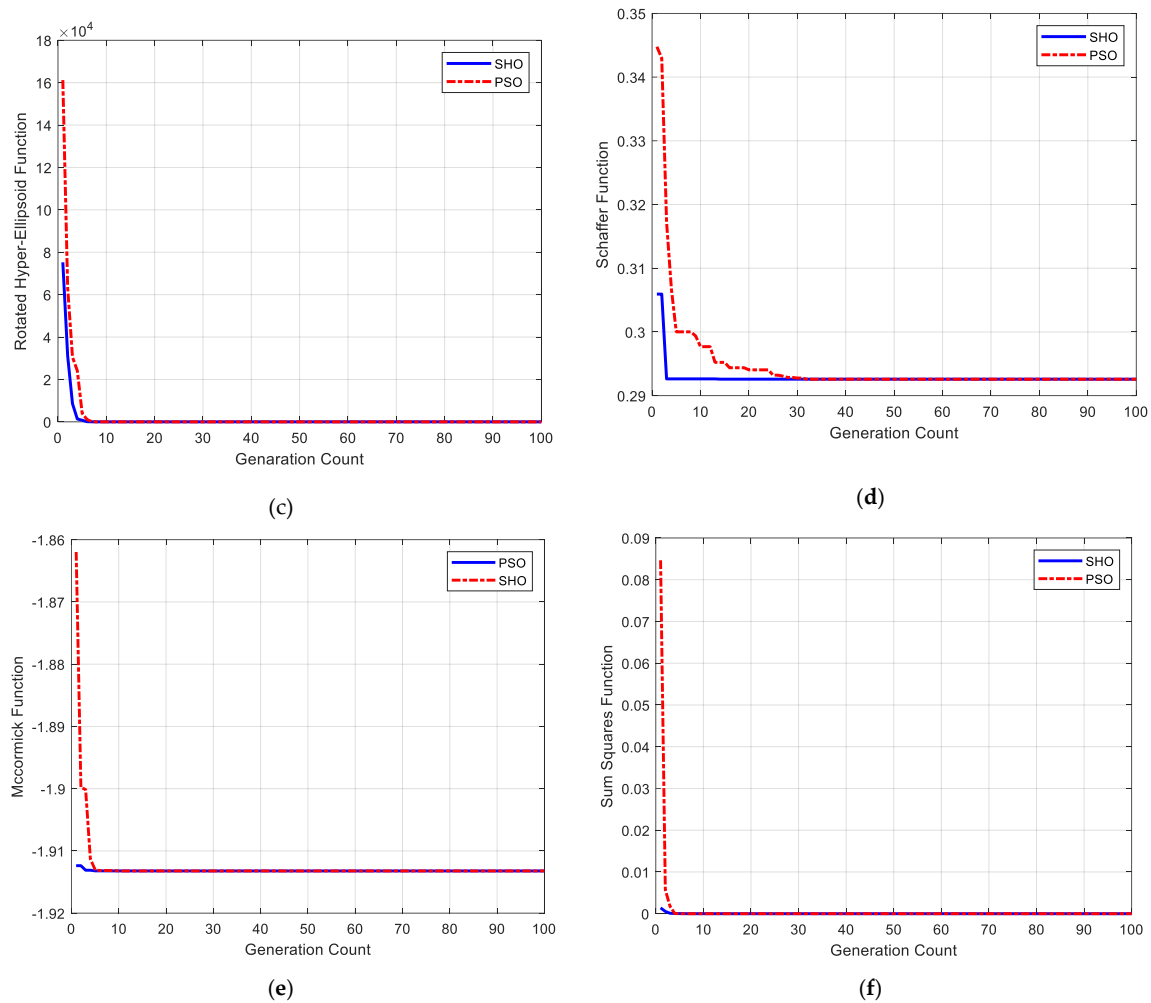


**Figure 5.** Convergence rate of SHO and PSO algorithms for different benchmark functions. (a) Hartmann function ( $F_1$ ). (b) Styblinski-Tang function ( $F_2$ ). (c) Rotated hyper-ellipsoid function ( $F_3$ ). (d) Schaffer function ( $F_4$ ). (e) McCormick function ( $F_5$ ). (f) Sum-squares function ( $F_6$ ).

**Table 2.** Specifications of different benchmark functions produced by SHO and PSO algorithms.

Functions	Optimum Value	Algorithm	Minimum Value	Maximum Value	Mean Value	Standard Deviation	Computation Time
F1	−3.862779	SHO	−3.862779	−3.8627795	−3.862779	$5.06756 \times 10^{-13}$	0.0907
		PSO	−3.862779	−3.8627795	−3.862779	$1.50773 \times 10^{-12}$	0.0545
F2	−78.332334	SHO	−78.332334	−78.332332	−78.33233	$4.78651 \times 10^{-14}$	0.06173
		PSO	−78.332334	−78.332331	−78.33233	$2.27205 \times 10^{-13}$	0.0429
F3	0	SHO	0	$4.06 \times 10^{-61}$	$1.42 \times 10^{-62}$	$7.40457 \times 10^{-62}$	0.2116
		PSO	0	$2.28 \times 10^{-55}$	$7.60 \times 10^{-57}$	$4.16291 \times 10^{-56}$	0.1199
F4	0.292578	SHO	0.292578	0.292584	0.292579	$1.11252 \times 10^{-6}$	0.1816
		PSO	0.292578	0.292582	0.292579	$1.12883 \times 10^{-6}$	0.1015
F5	−1.913334	SHO	−1.913334	−1.913334	−1.913334	$6.77522 \times 10^{-16}$	0.0644
		PSO	−1.913334	−1.913334	−1.913334	$6.77523 \times 10^{-16}$	0.0535
F6	0	SHO	0	$3.70 \times 10^{-105}$	$1.26 \times 10^{-106}$	$6.76254 \times 10^{-106}$	0.0753
		PSO	0	$6.74 \times 10^{-69}$	$2.24 \times 10^{-70}$	$1.23215 \times 10^{-69}$	0.0534

## 7. Results and Discussions

The simulation of the five-area test model has been established in the MATLAB/Simulink platform. Here, a disturbance of 0.01 puMW has been introduced to the system to investigate the transient effect. Observing the better convergence of SHO compared to PSO in the last section, here, in the first attempt, the effectiveness of the SHO-based PID controller over the PSO-based PID controller has been evaluated in the proposed test model. Then,

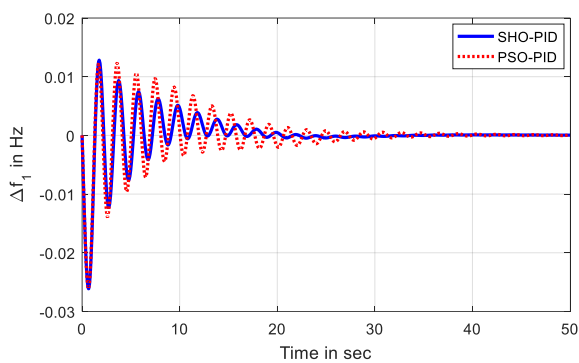
LFC of this model has been carried out through employing integer/non-integer controllers like PID and FOPID. Further, the additional benefits of a cascade controller with an FO operator have been evaluated and compared with the PID and FOPID controllers. To ensure an enhanced and robust performance, these controllers have been designed using a nascent and influential computational technique named SHO. Finally, to validate the system response, a real-time simulator has been applied. The designed values of these controllers have been provided in Table 3.

Table 3. Optimised controller gains.

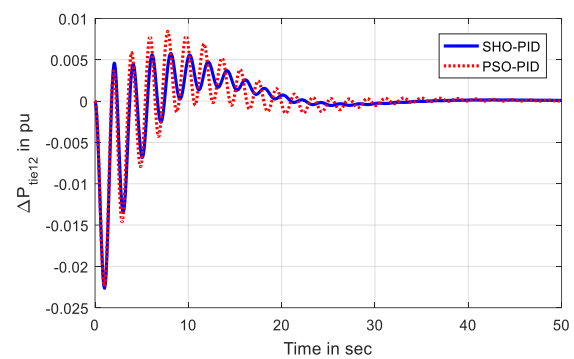
Controllers	Gains	Controller: -1	Controller: -2	Controller: -3	Controller: -4	Controller: -5	Controller: -6
PSO-PID	$k_p$	2.0100	3.7015	0.8841	2.3153	2.7354	4.7410
	$k_i$	2.8584	4.8286	1.2967	1.213	4.2418	1.9342
	$k_d$	0.917	3.022	1.415	2.4912	4.657	3.1582
SHO-PID	$k_p$	2.4489	3.7006	0.8842	2.4153	2.7354	4.7510
	$k_i$	2.5846	4.8287	1.2968	1.2138	4.2419	1.9340
	$k_d$	0.8170	3.0221	1.4125	2.4912	4.6571	3.1580
SHO-FOPID	$k_p$	1.7768	5.0000	3.2296	4.5374	3.3003	2.2579
	$k_i$	2.4797	4.4733	4.0218	5.0000	0.8270	4.0797
	$k_d$	0.1000	5.0000	5.0000	2.6260	5.0000	5.0000
	$\sigma$	0.9800	0.9800	0.5513	0.9800	0.9800	0.9800
	$\zeta$	0.9800	0.9800	0.9800	0.9800	0.9800	0.9710
SHO-FOPIDN-FOPDN	$k_{p1}$	0.5604	0.6463	0.8173	1.9264	1.7600	0.9897
	$k_{i1}$	2.1412	0.1889	0.0500	0.0500	0.7387	0.3839
	$k_{d1}$	0.0500	0.2034	2.2000	1.1085	0.8312	0.9342
	$k_{p11}$	1.4549	2.2000	0.6831	1.9451	0.5284	2.2000
	$k_{d11}$	0.0500	0.0500	2.0427	0.5276	1.4521	1.1862
	$N_1$	96.9082	150.0000	119.8054	70.6688	63.8810	74.4698
	$N_{11}$	101.3675	79.0033	85.6112	48.8753	110.7650	0.1000
	$\sigma_1$	0.6641	0.8500	0.7887	0.7203	0.4213	0.1000
	$\zeta$	0.1000	0.8500	0.5503	0.4230	0.7916	0.8500
	$\sigma_2$	0.1558	0.1000	0.2528	0.5132	0.7662	0.1586

7.1. Comparative Study of Transient Response Produced by SHO-PID and PSO-PID Controllers

In this case, a load perturbation has been given to the proposed model in the presence of a PID controller. The time-response curves of frequency and tie-line power have been presented in Figure 6. The SHO-PID controller has produced a better ameliorated response compared to PSO-PID. From this observation, it has been found that the SHO technique is better than the PSO technique. Various transient specifications have been given in Table 4. So, from this transient and convergence response, it has been perceived that the SHO technique has an upper hand to optimize a problem which has been corroborated in the rest of the work.



(a)



(b)

Figure 6. Cont.

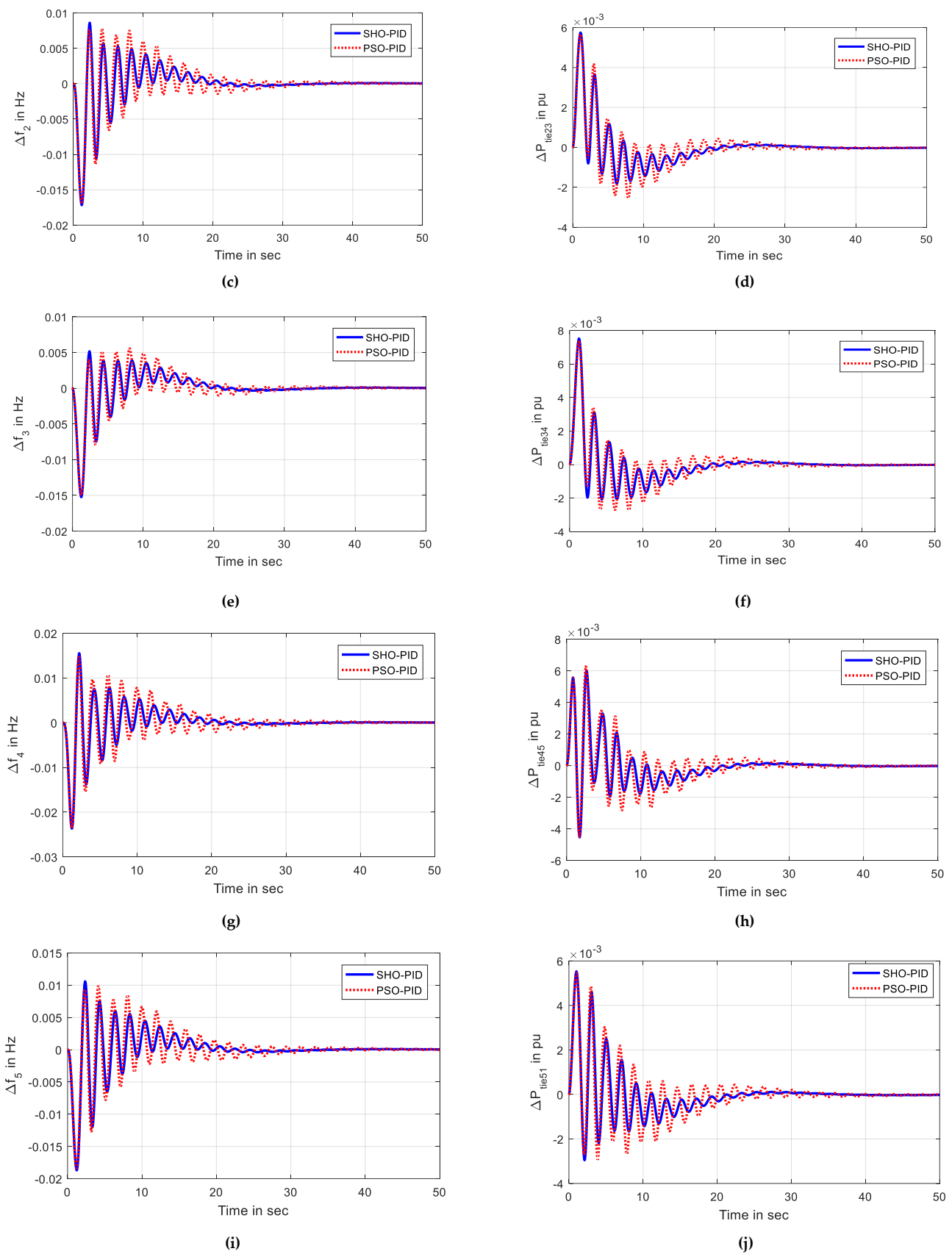


**Figure 6.** Deviation of frequency and tie-line power under SHO- and PSO-based PID controllers. (a) Frequency,  $\Delta f_1$  in area-1. (b) Tie-line power,  $\Delta P_{tie12}$  between area-1 and 2. (c) Frequency,  $\Delta f_2$  in area-2.

(d) Tie-line power,  $\Delta P_{tie23}$  between area-2 and 3. (e) Frequency,  $\Delta f_3$  in area-3. (f) Tie-line power,  $\Delta P_{tie34}$  between area-3 and 4. (g) Frequency,  $\Delta f_4$  in area-4. (h) Tie-line power,  $\Delta P_{tie45}$  between area-4 and 5. (i) Frequency,  $\Delta f_5$  in area-5. (j) Tie-line power,  $\Delta P_{tie51}$  between area-5 and 1.

**Table 4.** Specifications of deviation of frequency and tie-line power subjecting 1% step load in area-1 (Bold font represents superior results).

Controllers	Indices	$\Delta f_1$	$\Delta f_2$	$\Delta f_3$	$\Delta f_4$	$\Delta f_5$	$\Delta P_{tie12}$	$\Delta P_{tie23}$	$\Delta P_{tie34}$	$\Delta P_{tie45}$	$\Delta P_{tie51}$	ITAE
PSO-PID	$u_{sh} \times 10^{-3}$	-26.126	-16.971	-14.968	-23.547	-18.4469	-22.409	-2.5375	-2.7180	-4.5306	-2.9223	3.8215
	$o_{sh} \times 10^{-3}$	12.3120	7.8034	5.5810	14.9843	9.8836	8.4502	5.6681	7.3895	6.2866	5.4693	
	$t_s$ in sec	20.1623	17.7537	16.0183	20.6279	17.9168	42.838	26.5491	26.8182	30.0018	30.1412	
SHO-PID	$u_{sh} \times 10^{-3}$	-26.134	-17.180	-15.245	-23.659	-18.6990	-22.645	-1.8188	-2.0814	-4.5360	-2.9556	3.4664
	$o_{sh} \times 10^{-3}$	12.8190	8.6258	5.1715	15.5307	10.5826	5.7723	5.7534	7.5222	6.0164	5.5312	
	$t_s$ in sec	14.1857	14.7125	14.6414	14.7041	14.7585	31.931	18.6806	18.8061	20.3183	20.6083	
SHO-FOPID	$u_{sh} \times 10^{-3}$	-21.647	-13.459	-13.013	-18.105	-14.9512	-18.929	-0.9913	-0.9913	-0.7558	-0.9500	2.7372
	$o_{sh} \times 10^{-3}$	2.3614	2.2189	2.2185	2.1347	2.2183	3.2429	3.2429	5.2966	4.5344	4.7235	
	$t_s$ in sec	11.5900	12.0200	12.0300	11.5300	11.9800	31.938	17.5385	17.5385	22.3385	18.3385	
SHO-FOPIDN-FOPDN	$u_{sh} \times 10^{-3}$	<b>-20.938</b>	<b>-13.416</b>	<b>-13.005</b>	<b>-17.598</b>	<b>-15.8579</b>	<b>-18.468</b>	<b>-0.0880</b>	<b>-0.1380</b>	<b>-1.3762</b>	<b>0</b>	<b>0.7136</b>
	$o_{sh} \times 10^{-3}$	<b>0.6026</b>	<b>0.2743</b>	<b>0.2773</b>	<b>0.2524</b>	<b>0.2716</b>	<b>0.0343</b>	<b>5.2944</b>	<b>6.2322</b>	<b>4.4680</b>	<b>4.3739</b>	
	$t_s$ in s	<b>2.1935</b>	<b>2.7417</b>	<b>2.7417</b>	<b>2.1935</b>	<b>2.4787</b>	<b>11.042</b>	<b>6.9823</b>	<b>6.6650</b>	<b>11.7548</b>	<b>8.7749</b>	

7.2. Comparative Study of Transient Responses Produced by SHO Based Controllers without RFB

The system is investigated through subjecting it to a perturbation of 0.01 pu in area-1. The excursion of change in frequency and the excursion of change in tie-line power are portrayed in Figure 7. Performance parameters like undershoot ( $u_{sh}$ ), overshoot ( $o_{sh}$ ) and settling time ( $t_s$ ) of the responses are amassed in Table 4. Looking into the transient responses of different area-frequencies and tie-line powers, as depicted in Figure 7, conveys that the cascaded controller is more effective than the PID and FO-PID controllers. Inspecting the specifications amassed in Table 4, it is quite evident that the undershoot ( $u_{sh}$ ), overshoot ( $o_{sh}$ ) and settling time ( $t_s$ ) with the FOPIDN-FOPDN controller are very minimal with the comparison to its rivals. The ITAE cost function has a great role to minimize the error by which the gains of the different employed controllers are enumerated, culminating in an enriched dynamic and smooth performance. The ITAE values are 3.4664, 2.7372 and 0.7136 for the PID, FOPID and FOPIDN-FOPDN controller, respectively. So, in this work, the FOPIDN-FOPDN controller employing in the proposed system leaves behind other controllers' credibility.

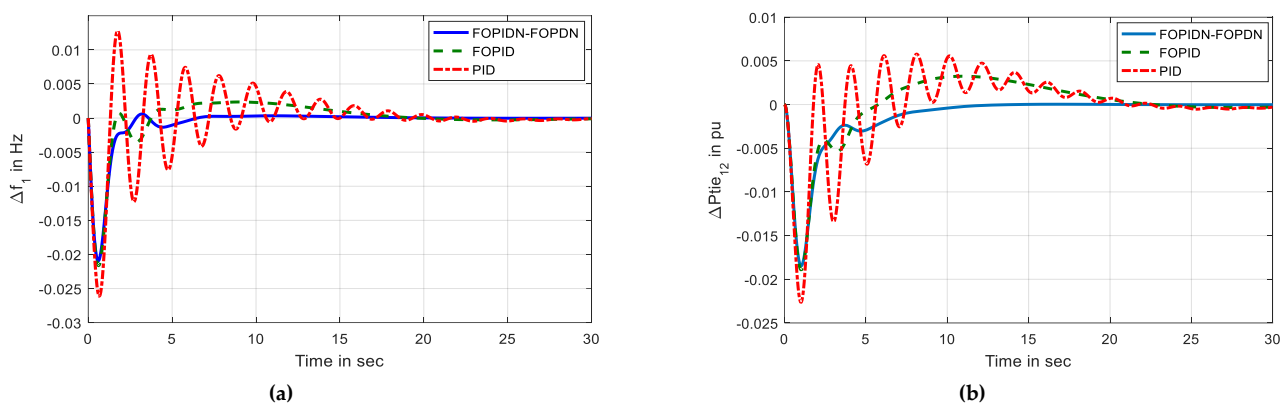
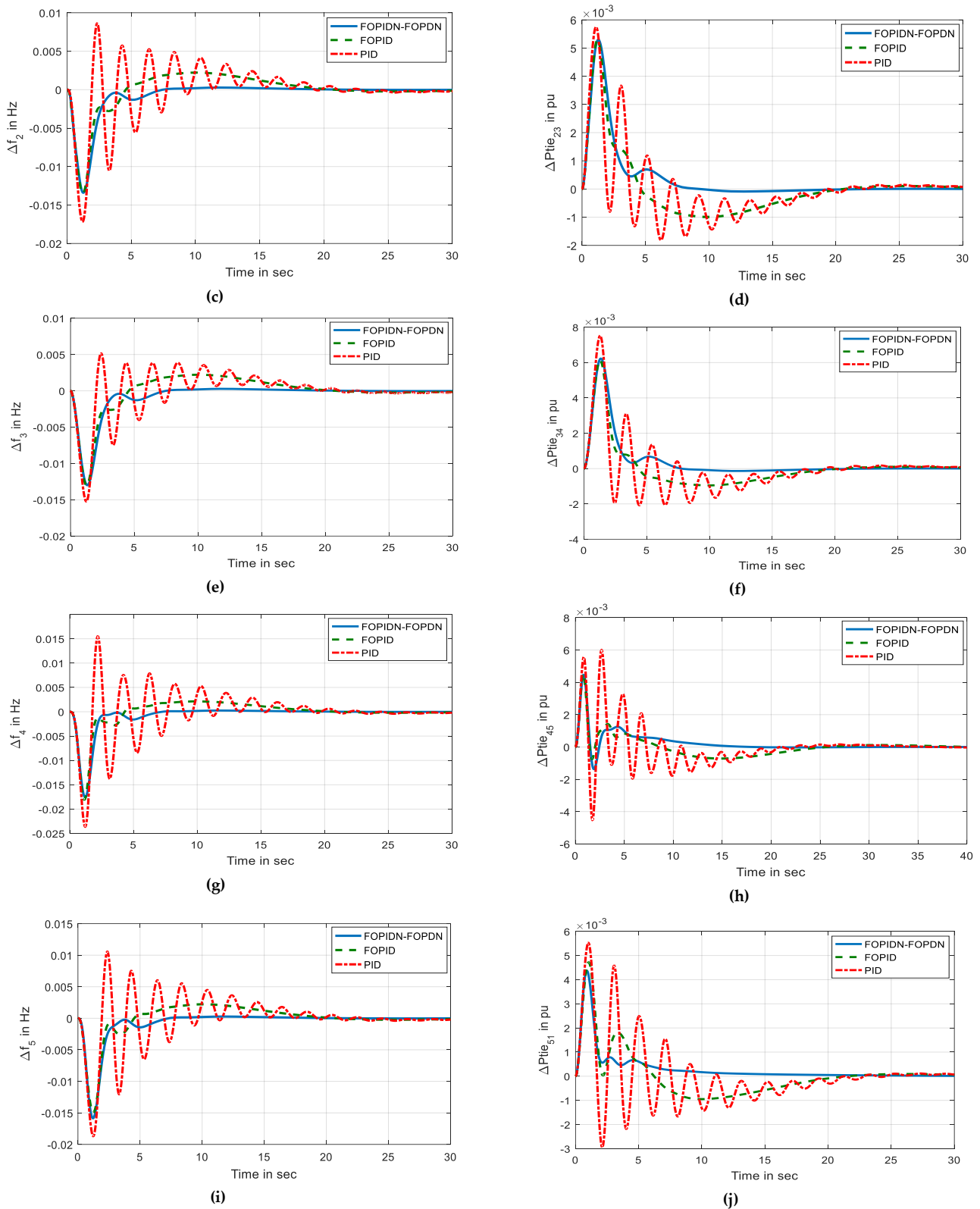


Figure 7. Cont.



**Figure 7.** Deviation of frequency and tie-line power under SHO based controllers without RFB integration in the system. (a) Frequency,  $\Delta f_1$  in area-1. (b) Tie-line power,  $\Delta P_{tie_{12}}$  between area-1 and 2. (c) Frequency,  $\Delta f_2$  in area-2. (d) Tie-line power,  $\Delta P_{tie_{23}}$  between area-2 and 3. (e) Frequency,  $\Delta f_3$  in area-3. (f) Tie-line power,  $\Delta P_{tie_{34}}$  between area-3 and 4. (g) Frequency,  $\Delta f_4$  in area-4. (h) Tie-line power,  $\Delta P_{tie_{45}}$  between area-4 and 5. (i) Frequency,  $\Delta f_5$  in area-5. (j) Tie-line power,  $\Delta P_{tie_{51}}$  between area-5 and 1.

### 7.3. Extension Work

Transient response of with RFB and Li-ion-based battery energy storage system (BESS).

To support the RFB technology in a large scale in a power system, another BESS (Li-ion) system has been considered in the proposed system. Here, a one-time constant model of a Li-ion battery [49–51] as shown in Figure 8 has been taken. The terminal voltage has been given in Equation (42). The transfer-function-based BESS model has been adapted from [52].

$$V_{batt}(t) = \frac{Q(0)}{C} e^{\left(\frac{-t}{RC}\right)} + V_{OC} - I_{batt}R_0 - I_{batt}R \left(1 - e^{\left(\frac{-t}{RC}\right)}\right) \quad (42)$$

where  $Q(0)$  = charge capacity of the cell and  $V_{OC}$  = nominal open circuit voltage, which depends on the state of charging.

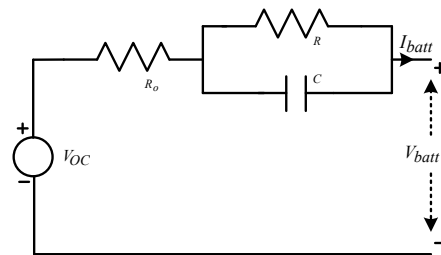


**Figure 8.** One-time constant model of Li-ion battery.

The test model has been integrated with an RFB and another BESS (Li-ion) system separately in all areas. The effect of these storage components with the proposed FOPIDN-FOPDN controller has been illustrated. The performance of the frequency deviation in area-1 and tie-line power deviation between area-1 and 2 with/without an RFB or BESS has been given in Figure 9. The peak values of undershoots for frequency and tie-line power deviation under an RFB are  $-5$  mHz and  $-6.7$  mpu, respectively. The FOPIDN-FOPDN controller with the RFB approach has improved the system response nearly four and 3 times for frequency and tie-line, respectively, which is more evident from Figure 9a,b. Simultaneously, the dynamic response of the RFB is better than the other BESS system, which is clear from the response presented in Figure 9.

### 7.4. Transient Response of the Test Model against Sporadic Load Variation under RFB

An arbitrary step load perturbation as depicted in Figure 10 is injected into the test model in area-1. Through endorsing the highly credible FOPIDN-FOPDN controller in the presence/absence of an RFB, the dynamic response has been evaluated. From this perspective, only the area-1 frequency deviation response and the tie-line power response traded off between area-1 and area-2, as illustrated in Figure 10. From Figure 10, it is quite noticeable that the unusual deviation in frequency and tie-line power die out within a very short-lived period. In addition to this, the peaks of undershoot/overshoot have been diminished significantly, which is obvious from the inset figure of Figure 10. So, the analysis suggests that the dynamic stability of the system remains intact and the robustness of the designed FOPIDN-FOPDN controller is firmly perceived through introducing an arbitrary step load variation in the presence of an RFB.

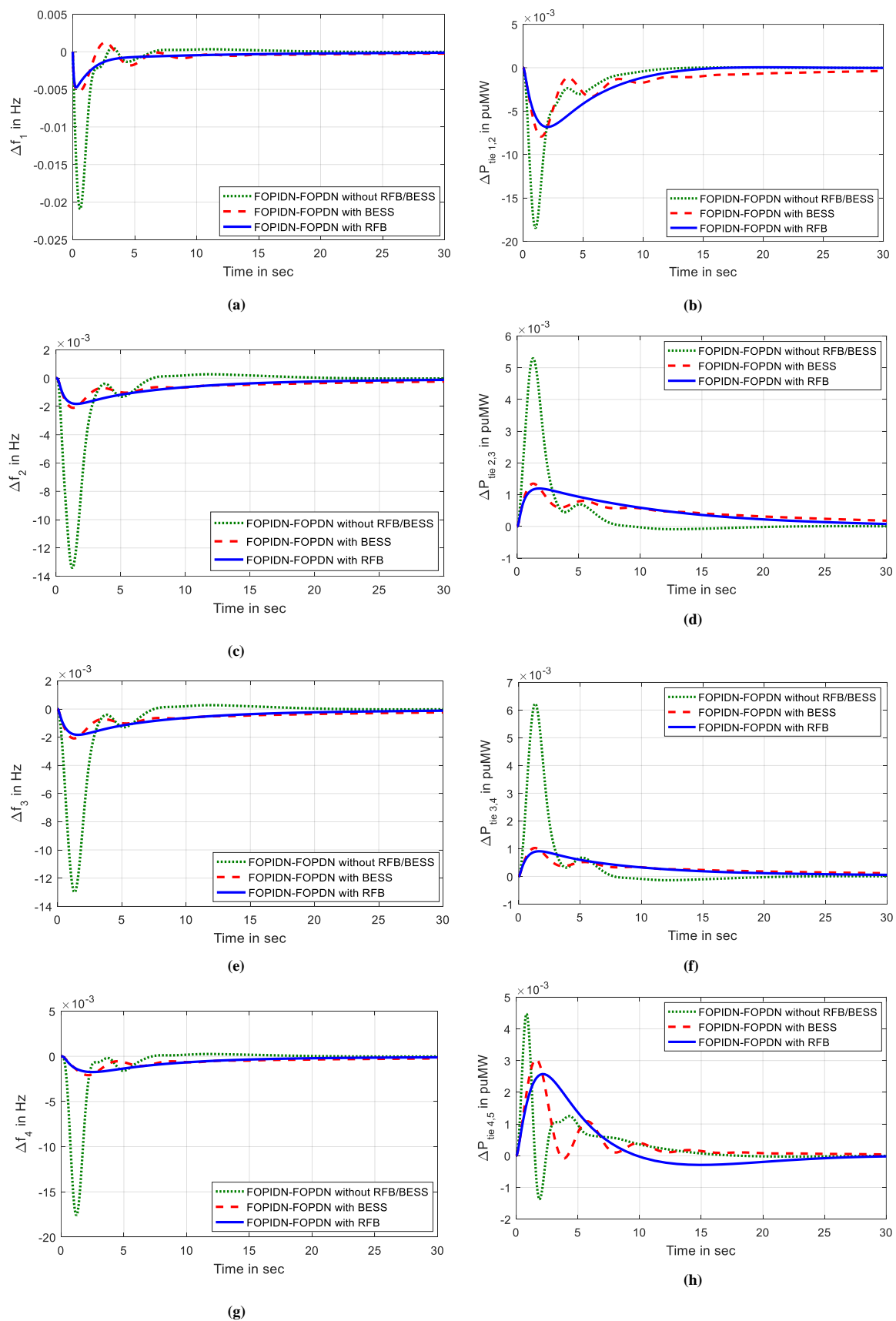
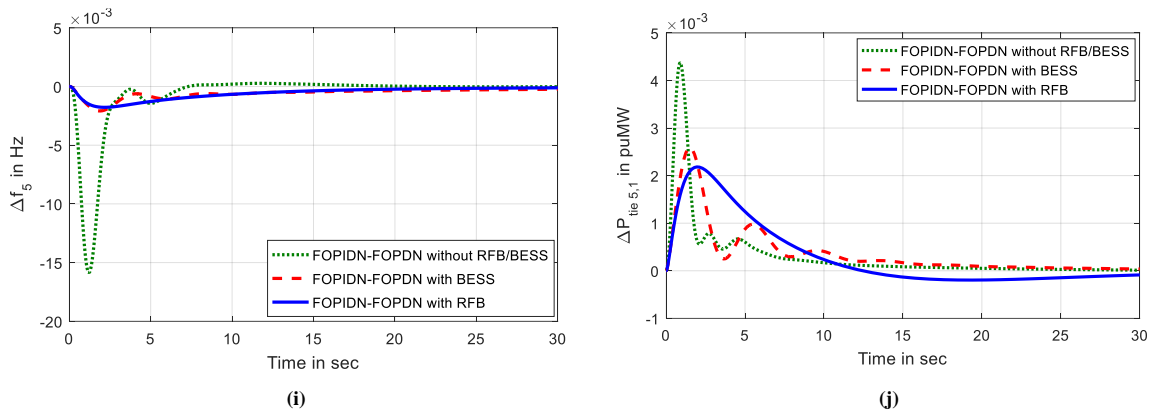
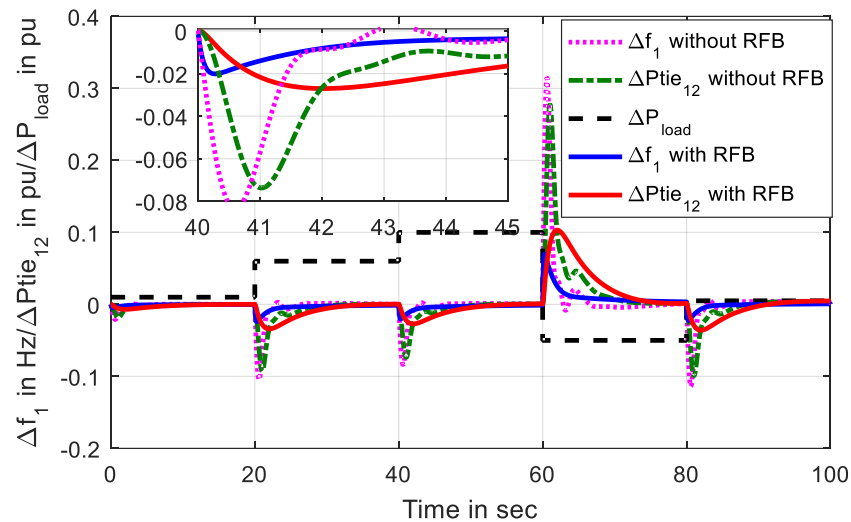


Figure 9. Cont.



**Figure 9.** Response of deviation of frequency and tie-line power. (a) Frequency,  $\Delta f_1$  in area-1. (b) Tie-line power,  $\Delta P_{tie_{12}}$  between area-1 and area-2. (c) Frequency,  $\Delta f_2$  in area-2. (d) Tie-line power,  $\Delta P_{tie_{23}}$  between area-2 and area-3. (e) Frequency,  $\Delta f_3$  in area-2. (f) Tie-line power,  $\Delta P_{tie_{34}}$  between area-3 and area-4. (g) Frequency,  $\Delta f_4$  in area-2. (h) Tie-line power,  $\Delta P_{tie_{45}}$  between area-4 and area-5. (i) Frequency,  $\Delta f_5$  in area-2. (j) Tie-line power,  $\Delta P_{tie_{51}}$  between area-5 and area-1.



**Figure 10.** Frequency and tie-line power deviation response against sporadic load variation.

7.5. Robustness of the Proposed FOPIDN-FOPDN Controller under RFB

Parameter variation during normal/disturbed operation of the power system is unavoidable, which affects the stability of the system immensely. But, this variation of parameters can be tightened using an optimally designed controller. To establish this, different crucial parameters of the system are varied keeping the same designed values of the FOPIDN-FOPDN controller as in Table 3. The responses measured via undershoot ( $u_{sh}$ ), overshoot ( $o_{sh}$ ) and settling time ( $t_s$ ) are given in Tables 5 and 6. Here, specifications of the frequency and tie-line power deviation are given in Tables 5 and 6, respectively. From these tables, it has been observed that the variation of these specifications is insignificant in comparison to the data observed under constant parameters as in Table 4. Along with this, the standard deviation of these specifications ( $o_{sh}/u_{sh}/t_s$ ), evaluated and presented in Tables 5 and 6, supports the potency of the controller adequately.

**Table 5.** Specifications of deviation in frequency after parametric variation.

Parameter Variation in %	$\Delta f_1$			$\Delta f_2$			$\Delta f_3$			$\Delta f_4$			$\Delta f_5$			
	$U_{sh} \times 10^{-3}$ (Hz)	$O_{sh} \times 10^{-3}$ (Hz)	$T_s$ (s)	$U_{sh} \times 10^{-3}$ (Hz)	$O_{sh} \times 10^{-3}$ (Hz)	$T_s$ (s)	$U_{sh} \times 10^{-3}$ (Hz)	$O_{sh} \times 10^{-3}$ (Hz)	$T_s$ (s)	$U_{sh} \times 10^{-3}$ (Hz)	$O_{sh} \times 10^{-3}$ (Hz)	$T_s$ (s)	$U_{sh} \times 10^{-3}$ (Hz)	$O_{sh} \times 10^{-3}$ (Hz)	$T_s$ (s)	
B	−20	−20.8286	0.7267	2.6384	−15.249	0.2985	3.1983	−14.7044	0.3024	3.1983	−19.4950	0.4253	3.0380	−17.6143	0.2970	3.1182
	−10	−20.8726	0.7984	2.5341	−14.248	0.2875	2.9472	−13.7965	0.2911	2.9472	−18.4848	0.2666	2.5980	−16.6816	0.2847	2.8446
	+10	−20.9991	0.3231	1.5176	−12.688	0.2580	2.5589	−12.3125	0.2609	2.5589	−16.8051	0.4785	2.1007	−15.1245	0.2530	2.2357
	+20	−21.0618	1.6159	1.4269	−12.067	0.2413	2.3863	−11.6996	0.2439	2.4776	−16.1019	1.4864	2.0827	−14.4684	0.3658	2.1586
R	−20	−21.0851	0.8645	1.6508	−13.329	0.2370	2.5511	−12.9019	0.2410	2.5511	−17.6109	0.2263	2.1123	−15.7778	0.2405	2.2519
	−10	−21.0034	0.7096	1.7651	−13.377	0.2559	2.6491	−12.9591	0.2590	2.6491	−17.6041	0.2394	2.1889	−15.8224	0.2577	2.3302
	+10	−20.8857	0.4975	2.3583	−13.447	0.2861	2.7609	−13.0403	0.2879	2.8601	−17.5930	0.2653	2.2947	−15.8862	0.2848	2.5819
	+20	−20.8418	0.4103	2.4673	−13.474	0.3003	2.8339	−13.0736	0.3024	2.9396	−17.5892	0.2751	2.3336	−15.9105	0.2957	2.6412
$T_{12}$	−20	−23.8967	3.5333	2.4711	−13.975	0.6453	2.5556	−13.5270	0.5202	2.5556	−18.7717	3.7212	4.5676	−16.7940	1.8802	2.3318
	−10	−22.2790	0.3481	1.6126	−13.667	0.2730	2.5864	−13.2497	0.2756	2.6826	−18.1363	1.2517	2.1867	−16.2851	0.2741	2.3466
	+10	−19.8070	0.5482	2.3590	−13.187	0.2749	2.8493	−12.7760	0.2775	2.9484	−17.1076	0.2551	2.6511	−15.4528	0.2726	2.8493
	+20	−18.8337	0.3236	2.4080	−12.988	0.2757	2.9282	−12.5650	0.2780	2.9282	−16.7056	0.2576	2.7369	−15.1052	0.2737	2.8326
$k_{ps}$	−20	−18.8372	0.6852	2.6743	−12.740	0.2742	2.9037	−12.3515	0.2768	3.0020	−16.6333	0.2520	2.3684	−15.0252	0.2710	2.5978
	−10	−19.9218	0.6323	2.4114	−13.107	0.2762	2.8040	−12.7042	0.2789	2.8997	−17.1481	0.2555	2.2629	−15.4692	0.2739	2.5598
	+10	−21.8991	0.5875	2.0478	−13.682	0.2712	2.6491	−13.2644	0.2744	2.6491	−18.0001	0.2484	2.1836	−16.2025	0.2685	2.4018
	+20	−22.8108	0.5798	1.8858	−13.912	0.2662	2.6287	−13.4954	0.2694	2.6287	−18.3579	0.2437	2.0832	−16.5006	0.2643	2.3803
$T_{ps}$	−20	−23.1771	0.5269	1.8448	−13.960	0.2606	2.5832	−13.5291	0.2638	2.5832	−18.4272	0.2386	2.1034	−16.5669	0.2593	2.3341
	−10	−21.9693	0.5658	2.0440	−13.678	0.2698	2.6544	−13.2610	0.2730	2.6544	−17.9949	0.2475	2.1810	−16.1985	0.2675	2.4020
	+10	−20.0328	0.6484	2.4185	−13.164	0.2732	2.7943	−12.7558	0.2755	2.8926	−17.2330	0.2539	2.2861	−15.5422	0.2727	2.5509
	+20	−19.2569	0.7009	2.5931	−12.924	0.2744	2.9193	−12.5279	0.2769	2.9193	−16.8946	0.2531	2.3641	−15.2380	0.2722	2.5931
$T_1$	−20	−20.9419	0.5990	2.1910	−13.415	0.2735	2.7381	−13.0038	0.2760	2.7381	−17.5993	0.2540	2.1910	−15.8593	0.2729	2.4764
	−10	−20.9398	0.5980	2.1993	−13.416	0.2747	2.7502	−13.0066	0.2775	2.7502	−17.5973	0.2540	2.1993	−15.8559	0.2730	2.4844
	+10	−20.9368	0.5979	2.1898	−13.415	0.2741	2.7366	−13.0031	0.2772	2.7366	−17.5968	0.2514	2.1898	−15.8580	0.2706	2.4753
	+20	−20.9349	0.6040	2.2535	−13.413	0.2752	2.7258	−12.9999	0.2780	2.8118	−17.5943	0.2544	2.1820	−15.8570	0.2734	2.4680
$T_2$	−20	−20.9310	0.6104	2.2491	−13.410	0.2876	2.7220	−12.9981	0.2905	2.8153	−17.5903	0.2666	2.2491	−15.8540	0.2857	2.4638
	−10	−20.9353	0.5994	2.1892	−13.002	0.2831	2.7357	−12.9971	0.2903	2.8227	−17.5954	0.2573	2.1892	−15.8568	0.2765	2.4747
	+10	−20.9407	0.5979	2.1986	−13.416	0.2693	2.7493	−13.0072	0.2721	2.7493	−17.5984	0.2487	2.1986	−15.8571	0.2677	2.4838
	+20	−20.9433	0.5916	2.1896	−13.416	0.2639	2.7361	−13.0041	0.2670	2.7361	−17.6005	0.2418	2.1896	−15.8610	0.2609	2.4750
$T_w$	−20	−20.944	0.6110	2.1935	−13.421	0.2748	2.7419	−13.0096	0.2775	2.7419	−17.6037	0.2548	2.1935	−15.8632	0.2738	2.4788
	−10	−20.9410	0.6069	2.1935	−13.418	0.2747	2.7418	−13.0073	0.2773	2.7418	−17.6007	0.2546	2.1935	−15.8604	0.2736	2.4788
	+10	−20.9363	0.5981	2.1935	−13.414	0.2742	2.7417	−13.0031	0.2769	2.7417	−17.5957	0.2542	2.1935	−15.8557	0.2731	2.4787
	+20	−20.9344	0.5937	2.1934	−13.412	0.2739	2.7416	−13.0014	0.2766	2.7416	−17.5936	0.2539	2.1934	−15.8537	0.2729	2.4787
Standard deviation	0.0535	0.0278	0.3198	0.0264	0.0033	0.149	0.0249	0.0022	0.1565	0.0326	0.0328	0.4552	0.0290	0.0142	0.1952	

**Table 6.** Specifications of deviation in tie-line power after parametric variation.

Parameter Variation in %	$\Delta P_{tie_{12}}$			$\Delta P_{tie_{23}}$			$\Delta P_{tie_{34}}$			$\Delta P_{tie_{45}}$			$\Delta P_{tie_{51}}$			
	$U_{sh} \times 10^{-3}$ (Hz)	$Osh \times 10^{-3}$ (Hz)	$T_s$ (s)	$U_{sh} \times 10^{-3}$ (Hz)	$Osh \times 10^{-3}$ (Hz)	$T_s$ (s)	$U_{sh} \times 10^{-3}$ (Hz)	$Osh \times 10^{-3}$ (Hz)	$T_s$ (s)	$U_{sh} \times 10^{-3}$ (Hz)	$Osh \times 10^{-3}$ (Hz)	$T_s$ (s)	$U_{sh} \times 10^{-3}$ (Hz)	$Osh \times 10^{-3}$ (Hz)	$T_s$ (s)	
B	-20	-17.5469	0.1832	6.2441	-0.0736	4.8783	2.6384	-0.1281	5.8105	2.7023	-1.1957	4.6184	1.2604	-0.0268	4.3445	1.4360
	-10	-18.0120	0.1819	6.1302	-0.0816	5.0926	2.4702	-0.1342	6.0304	2.5341	-1.2702	4.5356	1.2524	-0.0276	4.3539	1.4748
	+10	-18.9028	0.1799	5.9143	-0.0921	5.4877	2.3032	-0.1407	6.4189	2.3884	-1.4917	4.4144	1.2357	-0.0288	4.4009	1.5176
	+20	-19.3202	0.1790	5.7094	-0.0956	5.6664	2.2345	-0.1412	6.5931	2.3104	-1.6271	4.3786	1.2694	-0.0293	4.4421	1.4899
R	-20	-18.6795	0.1828	5.9466	-0.0699	5.3754	2.3217	-0.1224	6.3609	2.3915	-1.4586	4.4702	1.2650	-0.0266	4.4000	1.4928
	-10	-18.5622	0.1819	6.0339	-0.0769	5.3304	2.3302	-0.1304	6.2895	2.4008	-1.4127	4.4690	1.2624	-0.0275	4.3889	1.4919
	+10	-18.3928	0.1802	5.9398	-0.0979	5.2657	2.4220	-0.1429	6.1855	2.5019	-1.3452	4.4673	1.2577	-0.0289	4.3618	1.4681
	+20	-18.3296	0.1796	6.0059	-0.1057	5.2414	2.4005	-0.1481	6.1459	2.4673	-1.3135	4.4667	1.2581	-0.0294	4.3518	1.4718
$T_{12}$	-20	-19.3239	0.1803	5.9878	-0.0835	5.5859	2.3318	-0.1357	6.4976	2.4014	-2.1239	4.4762	3.5621	-0.0216	4.4883	1.6353
	-10	-18.8740	0.1807	5.8280	-0.0856	5.4343	2.3466	-0.1374	6.3596	2.4265	-1.7135	4.4700	1.3436	-0.0282	4.4242	1.5488
	+10	-18.1054	0.1812	6.0464	-0.0896	5.1721	2.4227	-0.1380	6.1163	2.4865	-1.0959	4.4782	1.1791	-0.0283	4.3325	1.4255
	+20	-17.7906	0.1813	5.8744	-0.0906	5.0601	2.5175	-0.1385	6.0090	2.5723	-0.8688	4.4890	1.1398	-0.0283	4.3034	1.3574
$k_{ps}$	-20	-18.1370	0.1810	5.9467	-0.0934	5.0654	2.5214	-0.1387	5.9379	2.6743	-1.7496	4.5919	1.3883	-0.0283	4.3887	1.6139
	-10	-18.3084	0.1808	5.9607	-0.0910	5.1900	2.4856	-0.1395	6.0969	2.5598	-1.5483	4.5264	1.3296	-0.0283	4.3798	1.5619
	+10	-18.6000	0.1808	5.9397	-0.0852	5.3881	2.3193	-0.1358	6.3483	2.4018	-1.215	4.4163	1.1915	-0.0282	4.3657	1.4431
	+20	-18.7181	0.1808	5.7847	-0.0821	5.4675	2.2147	-0.1319	6.4467	2.2975	-1.0781	4.3729	1.1269	-0.0282	4.3632	1.3797
$T_{ps}$	-20	-18.7159	0.1808	5.7230	-0.0806	5.4810	2.1681	-0.1302	6.4636	2.2511	-0.9898	4.3432	1.1174	-0.0282	4.3522	1.3682
	-10	-18.5873	0.1808	5.9085	-0.0845	5.3867	2.3179	-0.1347	6.3456	2.4020	-1.1867	4.4072	1.1848	-0.0282	4.3612	1.4359
	+10	-18.3547	0.1810	6.0270	-0.0916	5.2090	2.4185	-0.1391	6.1238	2.5509	-1.5442	4.5264	1.3175	-0.0283	4.3816	1.5238
	+20	-18.2446	0.1810	5.9759	-0.0936	5.1285	2.5168	-0.1394	6.0175	2.5931	-1.7109	4.5777	1.3486	-0.0283	4.3919	1.592
$T_1$	-20	-18.4708	0.1813	5.8303	-0.0883	5.2937	2.4050	-0.1360	6.2323	2.4764	-1.3784	4.4681	1.2575	-0.0284	4.3743	1.4870
	-10	-18.4671	0.1812	5.8762	-0.0880	5.2955	2.3418	-0.1375	6.2308	2.4844	-1.3751	4.4695	1.2659	-0.0283	4.3743	1.4971
	+10	-18.4692	0.1807	5.8974	-0.0875	5.2943	2.4039	-0.1386	6.2328	2.4753	-1.3764	4.4666	1.2556	-0.0282	4.3733	1.4848
	+20	-18.4688	0.1807	5.8766	-0.0881	5.2954	2.3965	-0.1378	6.2330	2.4680	-1.3767	4.4660	1.2510	-0.0282	4.3727	1.4772
$T_2$	-20	-18.4656	0.1750	5.8893	-0.0934	5.2952	2.3922	-0.1442	6.2322	2.4638	-1.3745	4.4657	1.2491	-0.0269	4.3718	1.4740
	-10	-18.4680	0.1779	5.8950	-0.0900	5.2942	2.4033	-0.1416	6.2325	2.4747	-1.375	4.4661	1.2551	-0.0276	4.3730	1.4840
	+10	-18.4684	0.1837	5.8743	-0.0858	5.2957	2.3412	-0.1347	6.2313	2.4838	-1.3760	4.4696	1.2653	-0.0289	4.3745	1.4963
	+20	-18.4729	0.1861	5.8927	-0.0832	5.2945	2.4037	-0.1331	6.2331	2.4750	-1.3798	4.4679	1.2557	-0.0294	4.3745	1.4848
$T_w$	-20	-18.4751	0.1800	5.8542	-0.0884	5.2962	2.4075	-0.1371	6.2344	2.4788	-1.3782	4.4692	1.2601	-0.0280	4.3752	1.4900
	-10	-18.4718	0.1805	5.8535	-0.0884	5.2953	2.4074	-0.1370	6.2332	2.4788	-1.3771	4.4686	1.2601	-0.0282	4.3745	1.4901
	+10	-18.4663	0.1815	5.8513	-0.0883	5.2937	2.4074	-0.1368	6.2312	2.4787	-1.3755	4.4676	1.2601	-0.0284	4.3734	1.4901
	+20	-18.4640	0.1820	5.8502	-0.0882	5.2930	2.4074	-0.1366	6.2303	2.4787	-1.375	4.4672	1.2601	-0.0285	4.3729	1.4901
Standard deviation	0.0176	$8.9 \times 10^{-5}$	0.1071	$3.42 \times 10^{-4}$	0.0078	0.0937	$2.42 \times 10^{-4}$	0.0083	0.0948	0.0118	0.0029	0.4126	$6.66 \times 10^{-5}$	0.0016	0.061	

### 7.6. Validation of the Transient Response through OPALRT (OP4510) Platform

The feasibility of the proposed model is simulated in the OPAL RT (OP4510) platform to validate the real-time dynamic response of different controllers. The real-time simulation set up has been given in Figure 11. The excursion of frequency/tie-line power deviation has been given in Figure 12. Figure 12 elucidates that the FOPIDN-FOPDN controller ameliorates the dynamic response of the PID and FOPID controllers, which is almost similar to the response observed in the MATLAB/SIMULINK environment.

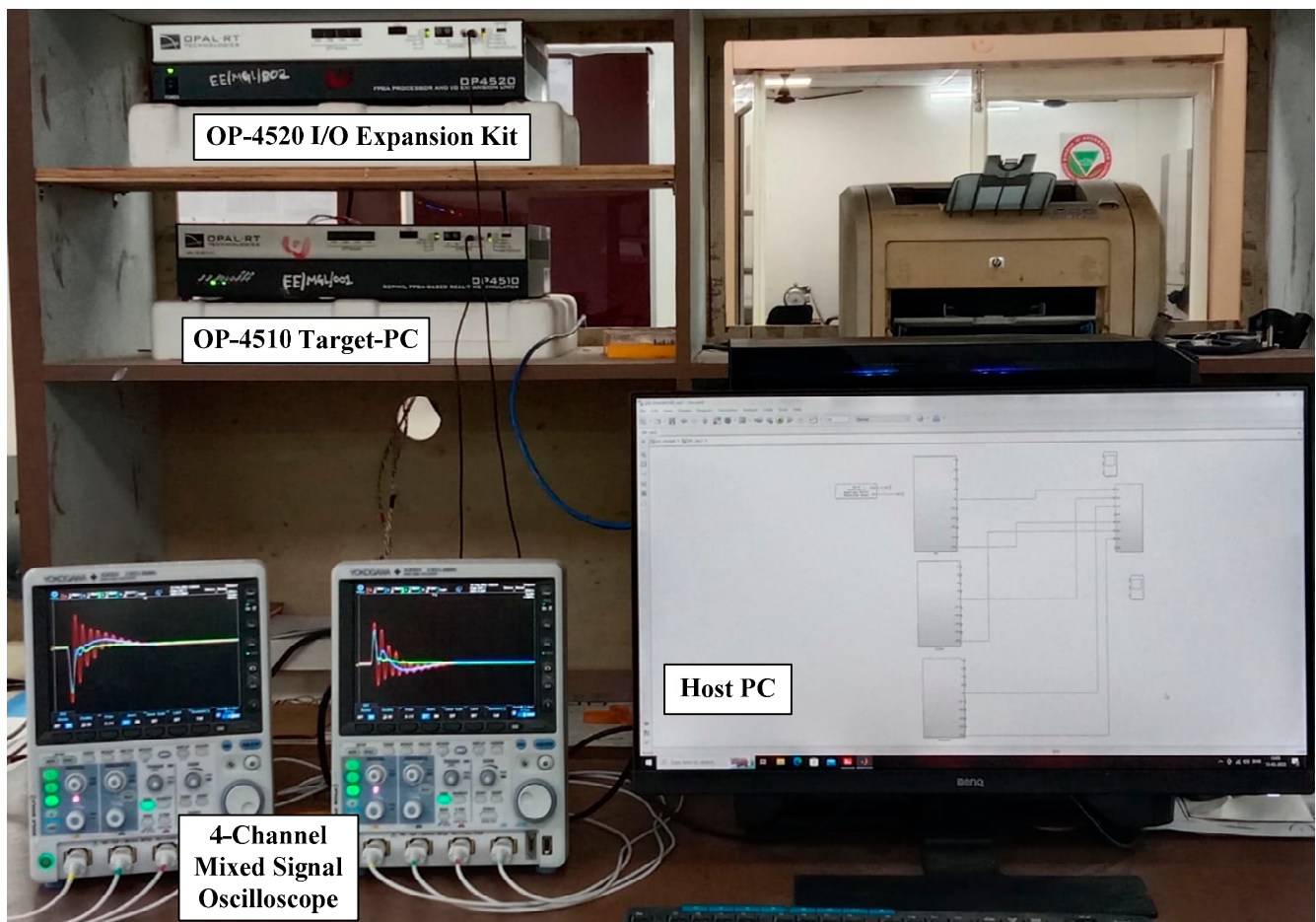


Figure 11. Experimental set up.

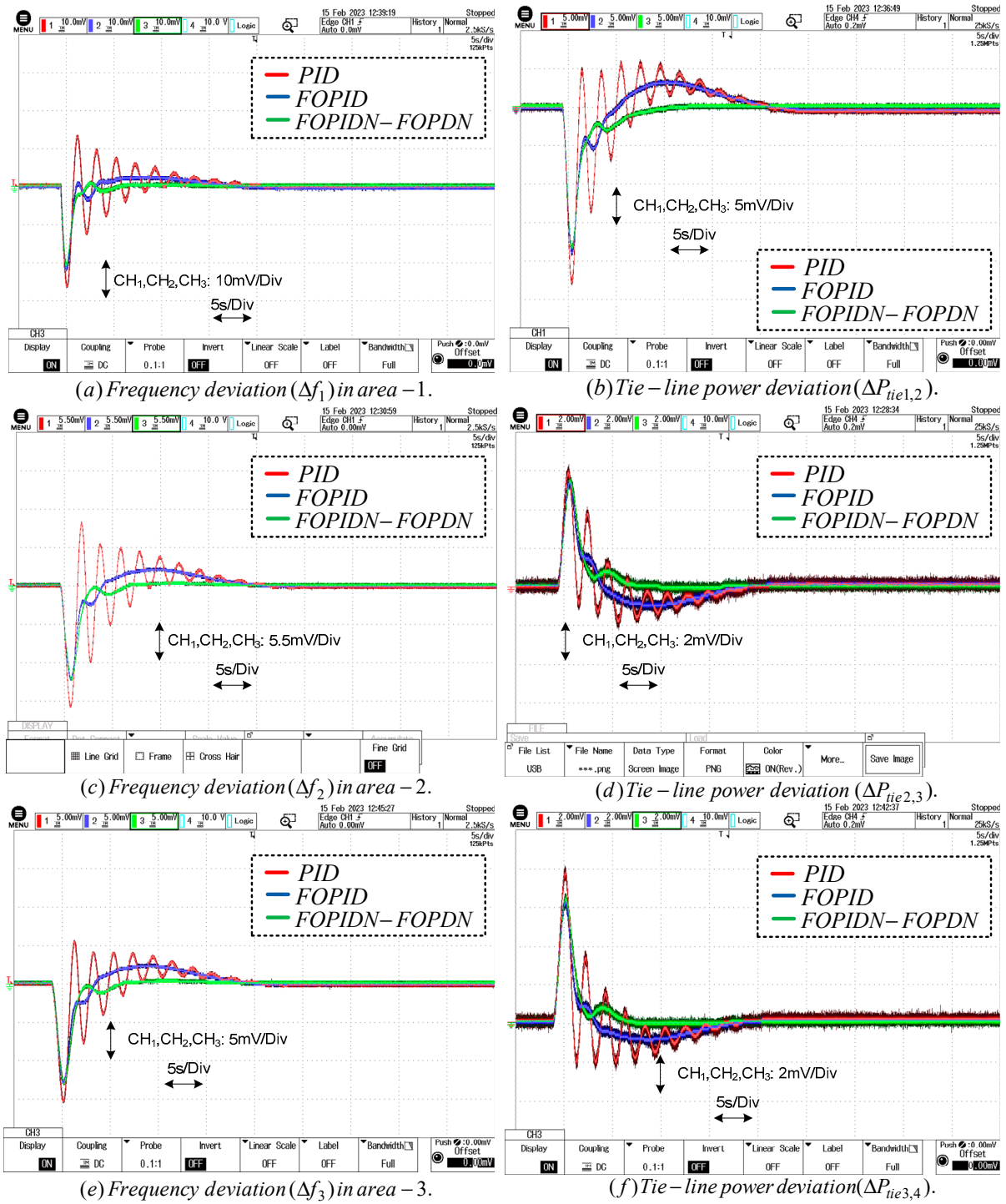


Figure 12. Cont.

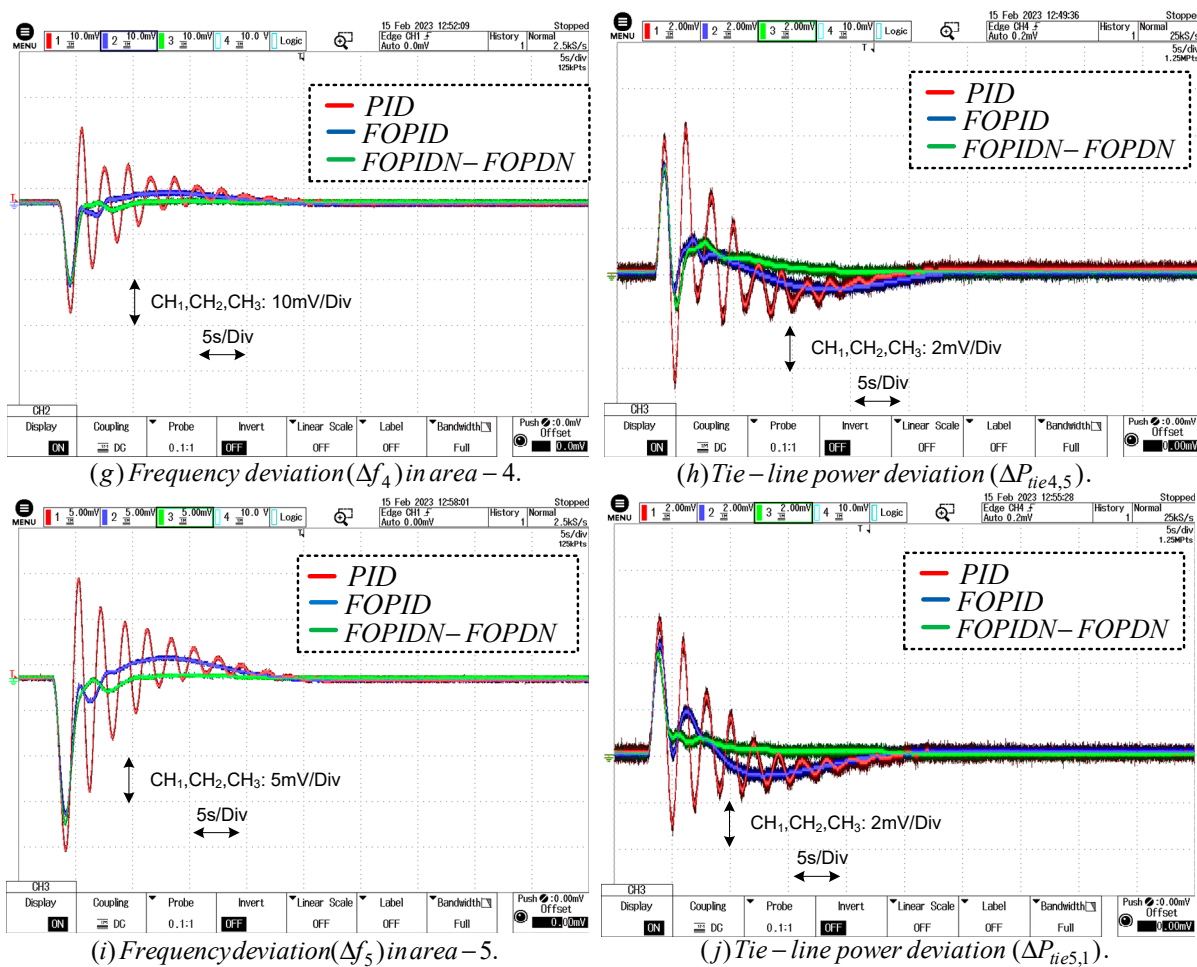


Figure 12. Frequency ( $\Delta f_1$ ) and tie-line power ( $\Delta P_{tie12}$ ) excursion.

## 8. Conclusions

In this comprehensive work, the LFC of the proposed system is intuited through enumerating different time domain specifications in a MATLAB/SIMULINK environment. AGC issues and the benefit of a secondary controller for this problem have been addressed prudentially. The ameliorated and prominent performance of the FOPIDN-FOPDN controller compared to the PID and FOPID controllers has been profoundly observed. The storage component, an RFB and another BESS system with a FOPIDN-FOPDN controller improved the dynamic response adequately. The SHO technique has shown better performance compared to PSO, as discussed in the benchmark analysis. The recommended SHO has gained an upper hand to evaluate the gains of controllers, by which the proposed controller has bestowed a fast and smooth response. The feasibility of the proposed controller is examined through simulating it in a real-time simulator, OPAL-RT (OP4510), which has given a similar response to that evaluated in the MATLAB platform. As the designed controller has preserved the stability of the system under chaotic step load perturbation and parametric variations of the system, hence, the robustness of the system affirms promisingly. Also, the RFB has strongly supported the dynamic response against sporadic load variation. In a nutshell, the proposed SHO-FOPIDN-FOPDN controller has stabilized the system remarkably, effortlessly and proficiently under normal/abnormal environments in the presence/absence of an RFB. Further, the AGC issues of this model can be addressed using fuzzy-logic-based intelligent controllers, sliding mode controllers and model predictive controllers under cyber threat or communication delay.

**Author Contributions:** Conceptualization, N.K.J., S.S., M.B., V.B. and L.P.; Methodology, N.K.J., A.K.N. and S.M.; Validation, N.K.J., S.S. and S.M.; Formal analysis, N.K.J., S.S. and M.B.; Investigation, B.K.S.; Resources, B.K.S. and V.B.; Data curation, A.K.N., V.B. and L.P.; Writing—review & editing, B.K.S., M.B. and V.B.; Supervision, M.B., S.M. and L.P.; Project administration, A.K.N., S.M. and L.P.; Funding acquisition, L.P. All authors have read and agreed to the published version of the manuscript.

**Funding:** These results were supported by projects LTI20004 “Environmental Research and Development Information Centre” funded by the Ministry of Education, Youth, and Sports of the Czech Republic; program INTER-EXCELLENCE, subprogram INTER-INFORM, and project TN02000025 National Centre for Energy II.

**Data Availability Statement:** Not applicable.

**Conflicts of Interest:** The authors declare no conflict of interest.

## Appendix A

Parameters are taken for different units

$$K_{ps} = 120, T_{ps} = 20s, R_x = R_y = 2.4, T_{12}, T_{13}, T_{14}, T_{15}, T_{23}, T_{24}, T_{25}, T_{34}, T_{35} \& T_{45} = 0.0707$$

$$a_{12}, a_{13}, a_{14}, a_{15}, a_{23}, a_{24}, a_{25}, a_{34}, a_{35} \& a_{45} = -1, B_1, B_2, B_3, B_4 \& B_5 = 0.425$$

Thermal Units:

$$T_{g1} = 0.2s, T_t = 0.3s, T_r = 10s, K_r = 0.333, N_1 = 0.8, N_2 = -0.2, K_1 = 0.85, K_2 = 0.095,$$

$$K_3 = 0.92, c_B = 200, K_{ib} = 0.5, T_{ib} = 26s, T_{rb} = 69s, T_D = 0, T_F = 10s, T_t = 0.3s.$$

Hydro Units:

$$T_{g,2} = 48.7s, T_1 = 0.513s, T_2 = 10s, T_w = 1s$$

Gas Unit:

$$C_{GS} = 1, B_{GS} = 0.05, X_{GS} = 0.6, Y_{GS} = 1, T_{CR} = 0.01s, T_{FR} = 0.23s, T_{CD} = 0.2s$$

Wind Farm and Diesel Unit:

$$k_2 = 1.25, k_3 = 1.4, T_{p1} = 0.6s, T_{p2} = 0.041s, k_{diesel} = 16.5.$$

Nuclear Unit:

$$T_{gn} = 0.03, k_{hn} = 2, T_{tn} = 0.5s, k_{rn} = 0.3, T_{rhn1} = 7s, T_{rhn2} = 9s$$

RFB component

$$K_{R.F.B.} = 1.8., T_{R.F.B.} = 0.$$

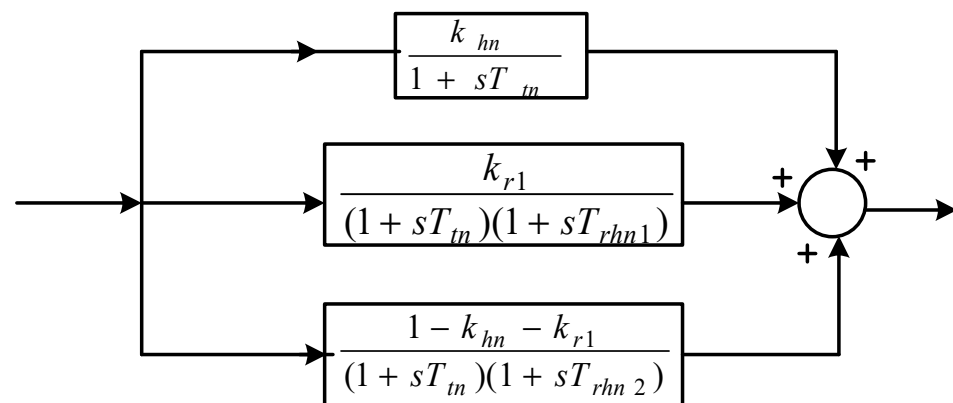


**Figure A1.** Nuclear power plant.

## References

1. Kundur, P.; Paserba, J.; Ajarapu, V.; Andersson, G.; Bose, A.; Canizares, C.; Hatziargyriou, N.; Hill, D.; Stankovic, A.; Taylor, C.; et al. Definition and Classification of Power System Stability IEEE/CIGRE Joint Task Force on Stability Terms and Definitions. *IEEE Trans. Power Syst.* **2004**, *19*, 1387–1401.
2. Elgerd, O.I.; Happ, H.H. Electric Energy Systems Theory: An Introduction. *IEEE Trans. Syst. Man Cybern.* **1982**, *2*, 296–297. [[CrossRef](#)]
3. Tripathy, S.; Balasubramanian, R.; Nair, P. Effect of superconducting magnetic energy storage on automatic generation control considering governor deadband and boiler dynamics. *IEEE Trans. Power Syst.* **1992**, *7*, 1266–1273. [[CrossRef](#)]
4. Nayak, A.; Maharana, M.K.; Panda, G. Frequency regulation of a RES integrated power system with AC/DC parallel link employing a fuzzy tuned fractional order controller. *Int. J. Emerg. Electr. Power Syst.* **2022**, *24*, 129–142. [[CrossRef](#)]

5. Nanda, J.; Mishra, S.; Saikia, L.C. Maiden Application of Bacterial Foraging-Based Optimization Technique in Multiarea Automatic Generation Control. *IEEE Trans. Power Syst.* **2009**, *24*, 602–609. [[CrossRef](#)]
6. Gozde, H.; Taplamacioglu, M.C. Automatic generation control application with craziness based particle swarm optimization in a thermal power system. *Int. J. Electr. Power Energy Syst.* **2011**, *33*, 8–16. [[CrossRef](#)]
7. Morsali, J.; Zare, K.; Tarafdar Hagh, M. MGSO optimised TID-based GCSC damping controller in coordination with AGC for diverse-GENCOs multi-DISCOs power system with considering GDB and GRC non-linearity effects. *IET Gener. Transm. Distrib.* **2017**, *11*, 193–208. [[CrossRef](#)]
8. Saikia, L.C.; Nanda, J.; Mishra, S. Performance comparison of several classical controllers in AGC for multi-area interconnected thermal system. *Int. J. Electr. Power Energy Syst.* **2011**, *33*, 394–401. [[CrossRef](#)]
9. Jagatheesan, K.; Anand, B.; Dey, K.N.; Ashour, A.S.; Satapathy, S.C. Performance evaluation of objective functions in automatic generation control of thermal power system using ant colony optimization technique-designed proportional–integral–derivative controller. *Electr. Eng.* **2018**, *100*, 895–911. [[CrossRef](#)]
10. Bhatt, P.; Roy, R.; Ghoshal, S. GA/particle swarm intelligence based optimization of two specific varieties of controller devices applied to two-area multi-units automatic generation control. *Int. J. Electr. Power Energy Syst.* **2010**, *32*, 299–310. [[CrossRef](#)]
11. Pandey, S.K.; Mohanty, S.R.; Kishor, N. A literature survey on load–frequency control for conventional and distribution generation power systems. *Renew. Sustain. Energy Rev.* **2013**, *25*, 318–334. [[CrossRef](#)]
12. Elgerd, O.I.; Fosha, C.E. Optimum Megawatt-Frequency Control of Multiarea Electric Energy Systems. *IEEE Trans. Power Appar. Syst.* **1970**, *4*, 556–563. [[CrossRef](#)]
13. Nayak, J.R.; Shaw, B.; Sahu, B.K.; Naidu, K.A. Application of optimized adaptive crow search algorithm based two degree of freedom optimal fuzzy PID controller for AGC system. *Eng. Sci. Technol. Int. J.* **2022**, *32*, 101061. [[CrossRef](#)]
14. Guha, D.; Roy, P.; Banerjee, S. Load frequency control of interconnected power system using grey wolf optimization. *Swarm Evol. Comput.* **2016**, *27*, 97–115. [[CrossRef](#)]
15. Gouran-Orimi, S.; Ghasemi-Marzbali, A. Load Frequency Control of multi-area multi-source system with nonlinear structures using modified Grasshopper Optimization Algorithm. *Appl. Soft Comput.* **2023**, *137*, 110135. [[CrossRef](#)]
16. Sahu, R.K.; Panda, S.; Rout, U.K.; Sahoo, D.K. Teaching learning based optimization algorithm for automatic generation control of power system using 2-DOF PID controller. *Int. J. Electr. Power Energy Syst.* **2016**, *77*, 287–301. [[CrossRef](#)]
17. Alomoush, M.I. Load frequency control and automatic generation control using fractional-order controllers. *Electr. Eng.* **2010**, *91*, 357–368. [[CrossRef](#)]
18. Morsali, J.; Zare, K.; Hagh, M.T. Applying fractional order PID to design TCSC-based damping controller in coordination with automatic generation control of interconnected multi-source power system. *Eng. Sci. Technol. Int. J.* **2017**, *20*, 1–17. [[CrossRef](#)]
19. Zamani, A.; Barakati, S.M.; Yousofi-Darmian, S. Design of a fractional order PID controller using GBMO algorithm for load–frequency control with governor saturation consideration. *ISA Trans.* **2016**, *64*, 56–66. [[CrossRef](#)]
20. Annamraju, A.; Bhukya, L.; Nandiraju, S. Robust frequency control in a standalone microgrid: An adaptive fuzzy based fractional order cascade PD-PI approach. *Adv. Control Appl. Eng. Ind. Syst.* **2021**, *3*, e72. [[CrossRef](#)]
21. Jena, N.K.; Sahoo, S.; Sahu, B.K.; Mohanty, K.B. Design of Fractional Order Cascaded Controller for AGC of a Deregulated Power System. *J. Control Autom. Electr. Syst.* **2022**, *33*, 1389–1417. [[CrossRef](#)]
22. Sivalingam, R.; Chinnamuthu, S.; Dash, S.S. A hybrid stochastic fractal search and local unimodal sampling based multistage PDF plus (1 + PI) controller for automatic generation control of power systems. *J. Frankl. Inst.* **2017**, *354*, 4762–4783. [[CrossRef](#)]
23. Saha, A.; Saikia, L.C. Performance analysis of combination of ultra-capacitor and superconducting magnetic energy storage in a thermal-gas AGC system with utilization of whale optimization algorithm optimized cascade controller. *J. Renew. Sustain. Energy* **2018**, *10*, 014103. [[CrossRef](#)]
24. Arya, Y. AGC of PV-thermal and hydro-thermal power systems using CES and a new multi-stage FPIDF-(1 + PI) controller. *Renew. Energy* **2019**, *134*, 796–806. [[CrossRef](#)]
25. Prakash, A.; Murali, S.; Shankar, R.; Bhushan, R. HVDC tie-link modeling for restructured AGC using a novel fractional order cascade controller. *Electr. Power Syst. Res.* **2019**, *170*, 244–258. [[CrossRef](#)]
26. Pahadasingh, S.; Chaine, S.; Priyadarshini, S.; Jena, C. LUS-TLBO Optimized Load Frequency Control for EV-Thermal-Hydro System Using Cascaded 3DOFPID-FOPID-FOPD-TID Controller. *J. Electr. Syst.* **2023**, *19*, 43–52.
27. Mao, J.; Liu, R.; Wu, A.; Wu, S.; He, J. An Improved Whale Optimization Algorithm Based PIDF-(1 + PI) Cascade Automatic Generation Control for Multi-area Multi-source Power System with Capacitive Energy Storage. *IEEE Access* **2023**.
28. Joseph, A.; Sobczak, J.; Żyła, G.; Mathew, S. Ionic Liquid and Ionanofluid-Based Redox Flow Batteries—A Mini Review. *Energies* **2022**, *15*, 4545. [[CrossRef](#)]
29. Arya, Y. AGC performance enrichment of multi-source hydrothermal gas power systems using new optimized FOPID controller and redox flow batteries. *Energy* **2017**, *127*, 704–715. [[CrossRef](#)]
30. Selvaraju, R.K.; Somaskandan, G. Impact of energy storage units on load frequency control of deregulated power systems. *Energy* **2016**, *97*, 214–228. [[CrossRef](#)]
31. Choudhary, R.; Rai, J.N.; Arya, Y. Cascade FOPI-FOPTID controller with energy storage devices for AGC performance advancement of electric power systems. *Sustain. Energy Technol. Assess.* **2022**, *53*, 102671. [[CrossRef](#)]
32. Shafei, M.A.R.; Ibrahim, D.K.; Bahaa, M. Application of PSO tuned fuzzy logic controller for LFC of two-area power system with redox flow battery and PV solar park. *Ain Shams Eng. J.* **2022**, *13*, 101710. [[CrossRef](#)]

33. Joshi, M.; Sharma, G.; Çelik, E. Load Frequency Control of Hydro-Hydro Power System using Fuzzy-PSO-PID with Application of UC and RFB. *Electr. Power Compon. Syst.* **2023**, *51*, 1156–1170. [[CrossRef](#)]
34. Kumar, V.; Sharma, V.; Naresh, R. Model predictive controller-based voltage and frequency regulation in renewable energy integrated power system coordinated with virtual inertia and redox flow battery. *Iran. J. Sci. Technol. Trans. Electr. Eng.* **2023**, *47*, 159–176. [[CrossRef](#)]
35. Sharma, M.; Dhundhara, S.; Sran, R.S. Impact of hybrid electrical energy storage system on realistic deregulated power system having large-scale renewable generation. *Sustain. Energy Technol. Assess.* **2023**, *56*, 103025. [[CrossRef](#)]
36. Wolpert, D.H.; Macready, W.G. No free lunch theorems for optimization. *IEEE Trans. Evol. Comput.* **1997**, *1*, 67–82. [[CrossRef](#)]
37. Abubakr, H.; Guerrero, J.M.; Vasquez, J.C.; Mohamed, T.H.; Mahmoud, K.; Darwish, M.M.F.; Dahab, Y.A. Adaptive LFC Incorporating Modified Virtual Rotor to Regulate Frequency and Tie-Line Power Flow in Multi-Area Microgrids. *IEEE Access* **2022**, *10*, 33248–33268. [[CrossRef](#)]
38. Sarma, U.; Saikia, L.C.; Sana, A.; Dash, P. Load frequency control of a multi-area, multi-source system using firefly algorithm optimized F2DOFIDD controller. In Proceedings of the 2016 IEEE Region 10 Conference (TENCON), Singapore, 22–25 November 2016; pp. 1475–1479.
39. Sahu, B.K.; Pati, S.; Mohanty, P.K.; Panda, S. Teaching–learning based optimization algorithm based fuzzy-PID controller for automatic generation control of multi-area power system. *Appl. Soft Comput.* **2015**, *27*, 240–249. [[CrossRef](#)]
40. Pradhan, C.; Bhende, C.N. Online load frequency control in wind integrated power systems using modified Jaya optimization. *Eng. Appl. Artif. Intell.* **2019**, *77*, 212–228. [[CrossRef](#)]
41. Fausto, F.; Cuevas, E.; Valdivia, A.; González, A. A global optimization algorithm inspired in the behavior of selfish herds. *Biosystems* **2017**, *160*, 39–55. [[CrossRef](#)]
42. Bhise, G.G.; Kothart, M.L.; Nanda, J. Optimum selection of hydrogovernor parameters for automatic generation control of a hydrothermal system. In Proceedings of the 1993 2nd International Conference on Advances in Power System Control, Operation and Management, APSCOM-93, Hong Kong, China, 7–10 December 1993; pp. 910–915.
43. Abdel-Magid, Y.; Abido, M. AGC tuning of interconnected reheat thermal systems with particle swarm optimization. 10th IEEE International Conference on Electronics, Circuits and Systems, 2003. ICECS 2003, Sharjah, United Arab Emirates, 14–17 December 2003; IEEE: Piscataway, NJ, USA, 2003; Volume 1, pp. 376–379.
44. Gozde, H.; Taplamacioglu, M.C.; Kocaarslan, I. Comparative performance analysis of Artificial Bee Colony algorithm in automatic generation control for interconnected reheat thermal power system. *Int. J. Electr. Power Energy Syst.* **2012**, *42*, 167–178. [[CrossRef](#)]
45. Shabani, H.; Vahidi, B.; Ebrahimpour, M. A robust PID controller based on imperialist competitive algorithm for load-frequency control of power systems. *ISA Trans.* **2013**, *52*, 88–95. [[CrossRef](#)] [[PubMed](#)]
46. Mohanty, B.; Prakash Kumar, H. Comparative performance analysis of fruit fly optimisation algorithm for multi-area multi-source automatic generation control under deregulated environment. *IET Gener. Transm. Distrib.* **2015**, *9*, 1845–1855. [[CrossRef](#)]
47. Podlubny, I. Fractional-order systems and PI/sup/spl lambda/ /D/sup/spl mu/ /-controllers. *IEEE Trans. Autom. Control* **1999**, *44*, 208–214. [[CrossRef](#)]
48. Oustaloup, A.; Levron, F.; Mathieu, B.; Nanot, F.M. Frequency-band complex noninteger differentiator: Characterization and synthesis. *IEEE Trans. Circuits Syst. Fundam. Theory Appl.* **2000**, *47*, 25–39. [[CrossRef](#)]
49. Sahoo, S.; Jena, N.K.; Ray, P.K.; Sahu, B.K. Selfish Herd Optimisation tuned fractional order cascaded controllers for AGC Analysis. *Soft Comput.* **2022**, *26*, 2835–2853. [[CrossRef](#)]
50. Rahmoun, A.; Biechl, H.; Rosin, A. Evaluation of Equivalent Circuit Diagrams and Transfer Functions for Modeling of Lithium-Ion Batteries. *Electr. Control Commun. Eng.* **2013**, *2*, 34–39. [[CrossRef](#)]
51. Liaw, B.Y.; Nagasubramanian, G.; Jungst, R.G.; Doughty, D.H. Modeling of lithium ion cells? A simple equivalent-circuit model approach. *Solid State Ion.* **2004**, *175*, 835–839.
52. Zhong, J.; He, L.; Li, C.; Cao, Y.; Wang, J.; Fang, B.; Zeng, L.; Xiao, G. Coordinated control for large-scale EV charging facilities and energy storage devices participating in frequency regulation. *Appl. Energy* **2014**, *123*, 253–262. [[CrossRef](#)]

**Disclaimer/Publisher’s Note:** The statements, opinions and data contained in all publications are solely those of the individual author(s) and contributor(s) and not of MDPI and/or the editor(s). MDPI and/or the editor(s) disclaim responsibility for any injury to people or property resulting from any ideas, methods, instructions or products referred to in the content.